Coral anthozoan-specific opsins employ a novel chloride counterion for spectral tuning

Yusuke Sakai[1], Saumik Sen[2,3], Tomohiro Sugihara[1], Yukiya Kakeyama[1], Makoto Iwasaki[1], Gebhard F.X. Schertler[4], Xavier Deupi[2,3,4,*], Mitsumasa Koyanagi[1,5,*], Akihisa Terakita[1,5,*]

1. Department of Biology, Graduate School of Science, Osaka Metropolitan University, Sumiyoshi-ku, Osaka 558-8585, Japan.
2. Condensed Matter Theory Group, Laboratory for Theoretical and Computational Physics, PSI Center for Scientific Computing, Theory, and Data, 5232 Villigen PSI, Switzerland.
3. Swiss Institute of Bioinformatics (SIB), Lausanne, Switzerland.
4. Laboratory of Biomolecular Research, PSI Center for Life Sciences, 5232 Villigen PSI, Switzerland.
5. The OMU Advanced Research Institute for Natural Science and Technology, Osaka Metropolitan University, Sumiyoshi-ku, Osaka 558-8585, Japan.

*Corresponding authors:

Xavier Deupi Email: xavier.deupi@psi.ch

Mitsumasa Koyanagi Email: koyanagi@omu.ac.jp

Akihisa Terakita Email: terakita@omu.ac.jp

Abstract

Animal opsins are G protein coupled receptors that have evolved to sense light by covalently binding a retinal chromophore via a protonated (positively charged) Schiff base. A negatively charged amino acid in the opsin, acting as a counterion, stabilizes the proton on the Schiff base, which is essential for sensitivity to visible light. In this study, we investigate the spectroscopic properties of a unique class of opsins from a reef-building coral belonging to the anthozoan-specific opsin II group (ASO-II opsins), which intriguingly lack a counterion residue at any of established sites. Our findings reveal that, unlike other known animal opsins, the protonated state of the Schiff base in visible light-sensitive ASO-II opsins is highly dependent on exogenously supplied chloride ions (Cl^-). By using structural modelling and QM/MM calculations to interpret spectroscopy data, we conclude that, in the dark state, ASO-II opsins employ environmental Cl^- as their native counterion, while a nearby polar residue, Glu292 in its protonated neutral form, facilitates Cl^- binding. In contrast, Glu292 plays a crucial role in maintaining the protonation state of the Schiff base in the light-activated protein, serving as the counterion in the photoproduct. Furthermore, Glu292 is involved in G protein activation of the ASO-II opsin, suggesting that this novel counterion system coordinates multiple functional properties.

35 # Introduction

36 Animals sense light by using opsins, photosensitive proteins belonging to the large family of G
37 protein-coupled receptors (GPCRs). These proteins have a seven-transmembrane helix structure and
38 bind to a retinal chromophore to form a light-sensitive pigment. Opsins are present in the genomes of
39 all eumetazoans (i.e., all animal lineages except sponges), and based on their phylogenetic
40 relationships, they can be classified into eight groups with distinctive properties: vertebrate visual/non-
41 visual opsins, opn3/TMT opsins, invertebrate Go-coupled opsins, cnidarian Gs-coupled opsins
42 (cnidopsins), neuropsins (opn5), Gq-coupled visual pigments/melanopsins (opn4), peropsins, and
43 retinochrome/RGR (Koyanagi and Terakita, 2014). Such diversity possibly underlies the
44 diversification of light-dependent physiologies in animals. Furthermore, this diversity also provides a
45 range of potential optogenetic tools to manipulate intracellular G protein-mediated signaling
46 (Koyanagi and Terakita, 2014).

47 Reef-building corals and sea anemones belong to the subphylum Anthozoa, which together
48 with the subphylum Medusozoa constitute the phylum Cnidaria. Cnidarian animals possess multiple
49 opsins categorized as part of the cnidarian Gs-coupled opsin group (cnidopsins), which regulate light-
50 dependent processes (Koyanagi et al., 2008). For example, a member of this group is expressed in the
51 ciliary type visual cells of the box jellyfish lens eyes (Koyanagi et al., 2008; Kozmik et al., 2008).
52 Beyond these Gs-coupled cnidopsins, anthozoan animals have opsins that are phylogenetically distinct
53 from the other known eight groups and are found exclusively in anthozoans (Feuda et al., 2012; Suga
54 et al., 2008). These anthozoan-specific opsins (ASO) can be further classified into two groups, ASO-I
55 and ASO-II (Gornik et al., 2020; Hering and Mayer, 2014; Mason et al., 2023; Picciani et al., 2018;
56 Ramirez et al., 2016). Gornik et al. (2021) proposed that both ASO-I and ASO-II were present in the
57 last common ancestor of Anthozoa and Medusozoa, but were lost secondarily in the Medusozoa
58 lineage (Gornik et al., 2020). While it has been reported that both ASO-I and ASO-II are expressed in
59 multiple tissues of sea anemones (Gornik et al., 2020; Suga et al., 2008) and corals (Levy et al., 2021),
60 there is still a limited understanding of their molecular characteristics and physiological functions.

The members of the ASO-II group are not only phylogenetically unique but also display interesting features in their amino acid sequences. For instance, several of these opsins lack an amino acid residue conserved among typical opsins that is crucial for absorption of visible light (Gornik et al., 2020; Mason et al., 2023). While free retinal in solution has its absorption maximum (λ_{max}) in the ultraviolet (UV), this shifts to visible light when retinal is bound to a lysine residue in the transmembrane bundle of the opsin (usually at Lys296, numbering according to the bovine rhodopsin sequence) through a protonated Schiff base to form the pigment. Such protonated Schiff base is necessary to achieve sensitivity to visible light in opsin-based pigments (Pitt et al., 1955). However, the proton on the positively charged Schiff base is energetically unstable in the hydrophobic transmembrane environment. To stabilize this proton, a negatively charged residue, glutamic or aspartic acid, is situated near the Schiff base to act as a counterion. This counterion is essential for opsin-based pigments to absorb visible light, and the residues serving as the counterion are highly conserved across opsins (Nathans, 1990; Terakita, 2005; Terakita et al., 2012). To date, three experimentally confirmed sites for the counterion have been identified in animal opsins: 94 in helix 2 (Gerrard et al., 2018), 113 in helix 3 (Nathans, 1990; Sakai et al., 2022; Sakmar et al., 1989; Zhukovsky and Oprian, 1989) and 181 in extracellular loop 2 (Nagata et al., 2019; Terakita et al., 2004, 2000). Remarkably, some opsins belonging to the ASO-II group lack glutamic or aspartic acid at any of these established counterion positions (Gornik et al., 2020; Mason et al., 2023). This absence raises the question of whether these opsins can absorb visible light, and if so, by what mechanism.

In this study, we investigate the spectroscopic properties of opsins in the ASO-II group isolated from the reef-building coral *Acropora tenuis*. Absorption spectra reveal that this group includes opsins sensitive to both UV and visible light. We then focus on a particular visible light-sensitive opsin within the ASO-II group (Antho2a) by spectroscopically analyzing the protonated and deprotonated states of the Schiff base in the wild type and in single point mutants. By interpretating the spectroscopy data in the light of hybrid quantum mechanics/molecular mechanics (QM/MM) simulations, we demonstrate that a chloride anion (Cl^-) serves as a counterion to the retinylidene Schiff base in animal opsins, specifically in visible light-sensitive opsins of the ASO-II group.

88

89 # Results

90 **Identification of *Acropora tenuis* opsins**

91 We identified 17 opsins from the *Acropora tenuis* genome and transcriptome datasets by homology
92 search, which included eight opsins in Gs-coupled cnidopsin group, one opsin in the ASO-I group, and
93 eight opsins in the ASO-II group (Fig. S1; Fig. 1A). Full-length cDNAs of seven out of the eight
94 opsins in the ASO-II group were isolated and cloned from adult or larval tissues of the coral
95 (highlighted by bold letters in Fig. 1A). We failed to amplify one opsin in the ASO-II group (gene
96 model ID in the OIST Marine Genomics Unit Genome Project (Shinzato et al., 2020):
97 aten_s0263.g14) by RT-PCR possibly because of its little mRNA expression level. Amino acid
98 sequence alignment shows that all the seven *A. tenuis* opsins in the ASO-II group lack a glutamic or
99 aspartic acid at the established counterion positions 94, 113 or 181 (Fig. 1B; Fig. S2). These opsins
100 also have no E(D)RY motif at the cytoplasmic end of helix 3 (Fig. S2), which is conserved throughout
101 most class A GPCRs (Hofmann et al., 2009).

102

103 **Absorption spectra of *Acropora tenuis* opsins in the ASO-II group**

104 We expressed seven members of the ASO-II group in COS-1 cells and purified their recombinant
105 pigments in detergent-solubilized conditions. We successfully obtained the absorption spectra of three
106 (Antho2a, Antho2c and Antho2e) out of the seven members, which showed that Antho2a and Antho2c
107 are visible light-sensitive opsins having with λ_{max} at 503 nm and 450 nm, respectively, whereas
108 Antho2e is a UV-sensitive opsin with λ_{max} at ~360 nm (Fig. 1C). We have previously reported that one
109 opsin in the ASO-II group, acropsin 4 of the coral *Acropora millepora*, induces a light-dependent
110 elevation of intracellular Ca^{2+} levels (Mason et al., 2023). Here, we showed that Antho2a, Antho2c and
111 Antho2e evoked a similar light-dependent increase of Ca^{2+} levels in HEK293S cells (Fig. 1D).

112

113 **Search for the counterion in *Acropora tenuis* opsins of the ASO-II group**

114 Antho2a and Antho2c form visible light-sensitive pigments in the dark (Fig. 1C) despite the lack of a
115 negatively charged counterion at any of the established positions (Fig. 1B; Fig. S2). To investigate
116 how the protonated Schiff base is stabilized in these opsins, we studied in more detail Antho2a (λ_{max} =
117 503 nm), as it could be expressed well in cultured cells and was stable in detergent-solubilized
118 conditions (Fig. 1C).
119
120 *(a) Contribution of Glu292 to the absorption spectra of the dark state and photoproduct of Antho2a*
121 First, we searched for potential counterions at positions different from known established amino acid
122 sites (91, 113, and 181) in the Antho2a sequence. Using the crystal structure of bovine rhodopsin
123 (PDB ID: 1U19) as a template, we identified glutamic or aspartic acids located within 5Å of the Schiff
124 base in Antho2a and other members in the ASO-II group. Notably, all *A. tenuis* opsins in this group
125 contain a conserved glutamic/aspartic acid at position 292 (Fig. 1B; Fig. S2), positioned just one helix
126 turn away from the retinal-binding residue Lys296. To determine whether Glu292 could function as
127 the counterion in Antho2a, we mutated Glu292 to alanine and measured the absorption spectra. The
128 absorption spectrum of the E292A mutant in the dark was nearly identical to that of wild type (Fig.
129 2A, B, curve 1), exhibiting a clear absorbance in the visible light region with only a slightly red-
130 shifted λ_{max} (505 nm) at 140 mM NaCl and pH 6.5. This shows that a negative charge other than
131 Glu292 may serve as a counterion in the dark state of wild type Antho2a.
132 We next investigated the spectroscopic properties of the photoproduct of wild type Antho2a and
133 the E292A mutant. Upon irradiation of wild type Antho2a with orange light, the λ_{max} shifted from 503
134 nm in the dark to 476 nm in the photoproduct (Fig. 2A, curve 2; Fig. S3A, curves 2 and 3). This shift
135 is due to the photoisomerization of the 11-*cis* retinal chromophore to its all-*trans* form, converting
136 almost 100% of the dark state to the photoproduct (Fig. S3B). The photoproduct remained stable for at
137 least 5 minutes (Fig. S3A, curves 2 and 3) but did not revert to the original dark state upon subsequent
138 irradiation (Fig. S3A and C). Instead, it underwent gradual decay accompanied by retinal release over
139 time (Fig. S3D–G). These findings indicate that purified Antho2a is neither strictly bleach resistant nor
140 bistable (see also Fig. S3 legend). We also observed that the protonated photoproduct decayed more

141 rapidly at pH 8.0 (Fig. S3H) than at pH 6.5 (Fig. 3A, D, E). In contrast to the dark state, the
142 photoproduct of the E292A mutant displayed two distinct absorption peaks in UV and visible light
143 regions, at ~370 nm and 476 nm, respectively (Fig. 2B, curve 2). This suggests that the E292A
144 mutation causes UV-light absorption due to a deprotonated Schiff base in the photoproduct.
145 Additionally, altering the pH modified the ratio of absorbance between the ~370 nm and 476 nm peaks
146 in the E292A mutant (Fig. S4B, curves 2), with the UV-peak to the visible light-peak ratio increasing
147 at higher pH levels (pH 7.4, Fig. S4B, curve 2). Conversely, the wild type did not exhibit an increase
148 in UV absorbance under similar high pH condition (pH 7.5, Fig. S4A, curve 2). These results indicate
149 that the Schiff base in the photoproduct of the Antho2a E292A mutant has a lower acid dissociation
150 constant (pK_a) than that of the wild type, suggesting that Glu292 acts as the counterion in the
151 photoproduct of Antho2a.
152 We then further explored the nature of the counterion in the dark state of Antho2a. Previous
153 studies have shown that in the bovine rhodopsin E113A and E113Q mutants, as well as in the
154 retinochrome E181Q mutant (referred to as "counterion-less" mutants), halide ions like Cl^- can act as
155 "surrogate" counterions to stabilize the proton on the Schiff base. Consequently, these counterion-less
156 mutants can still absorb visible light in the presence of Cl^- (Nathans, 1990; Sakmar et al., 1991;
157 Terakita et al., 2000). To assess the potential role of Cl^- as a surrogate counterion in the dark state of
158 the Antho2a E292A mutant, we performed spectroscopic analyses under Cl^--depleted conditions (Fig.
159 2C, D). We observed that the λ_{max} of the E292A mutant shifted to the UV region (Fig. 2D, curve 1).
160 Unexpectedly, a similar shift in absorption to the UV region was also observed in the wild type under
161 the Cl^--depleted condition (Fig. 2C, curve 1). These results indicate that, in the absence of Cl^-, the
162 Schiff base in both the wild type and the E292A dark states becomes deprotonated. The subsequent
163 addition of Cl^- (final concentration: 140 mM NaCl) restored clear absorbance in the visible light
164 region (Fig. 2C, D, curves 2), showing that Cl^- facilitates the protonation of the Schiff base of the dark
165 state even in the wild type. In contrast, the photoproduct of the wild type exhibited no significant
166 change in the ratio of UV to visible-light absorption peaks at pH 6.5 across NaCl concentrations from
167 0.28 mM to 800 mM (Fig. S5). The photoproduct of the wild type consistently absorbed visible light

168 under these NaCl conditions (curves 2 in Fig. S5A, B), suggesting that Cl^- has little impact on the
169 Schiff base pK_a in the photoproduct of wild type Antho2a. However, the photoproduct of the E292A
170 mutant exhibited a pH-dependent shift in the ratio of UV to visible-light absorption between pH 4.8
171 and pH 7.6, even at 800 mM NaCl, where the dark state predominantly absorbed visible light (Fig.
172 S5C). This further supports that Glu292 serves as the counterion in the photoproduct of Antho2a.
173
174 *(b) Effect of halide anions on λ_{max} values of the dark state of Antho2a*
175 To obtain a further evidence supporting the Cl^- counterion in the dark state of Antho2a, we examined
176 the impact of different halide anions on the absorption spectrum in the dark state of Antho2a, as
177 observed in the bovine rhodopsin counterion-less mutant (Nathans, 1990; Sakmar et al., 1991).
178 Antho2a readily absorbed visible light in the presence of bromide ion (Br^-) and iodide ion (I^-) as well
179 as Cl^- and the λ_{max} of wild type Antho2a shifted depending on the halide solutions (503 nm in 140 mM
180 NaCl; 506 nm in 140 mM NaBr; 511 nm in 140 mM NaI solutions; Fig. 2E). The E292A mutant
181 showed a similar shift in λ_{max} (505 nm in 140 mM NaCl; 507 nm in 140 mM NaBr; 517 nm in 140
182 mM NaI solutions; Fig. 2F).
183
184 *(c) Effect of Cl^- concentration on the pK_a of the protonated Schiff base of Antho2a*
185 To further investigate the influence of Cl^- on the protonation state of the Schiff base in the dark state
186 of Antho2a, we estimated the pK_a of the Schiff base by measuring the pH-dependent changes in the
187 absorption spectra of Antho2a at different Cl^- concentrations. The pH-dependent equilibrium between
188 the visible (protonated Schiff base) and UV (deprotonated Schiff base) forms revealed that their ratio
189 changes with Cl^- concentration (Fig. S6A–E). A plot of the changes in absorbance at λ_{max} against pH
190 (Fig. 3A) shows that in wild type Antho2a, the pK_a of the protonated Schiff base increases with higher
191 Cl^- concentrations (7.3 at 0.28 mM NaCl, 8.0 at 2.8 mM, 8.8 at 28 mM, 8.8 at 140 mM, and 9.0 at 500
192 mM). We failed to determine the pK_a at 0 mM NaCl, as the observed λ_{max} in acidic conditions (pH <
193 6.5) were shorter than expected in Antho2a (503 nm), suggesting that a normal pigment was not
194 produced under these conditions (Fig. S7A). Similarly, the Cl^- concentration also affected the pK_a of

195 the protonated Schiff base in the E292A mutant (6.1 at 2.8 mM NaCl, 6.8 at 28 mM, 7.7 at 140 mM,
196 and 8.9 at 500 mM) (Fig. 3B; Fig. S8). At 0 mM NaCl, the E292A mutant showed no visible light
197 absorption, even under the most acidic conditions (pH 4.7), preventing the determination of its pK_a
198 (Fig. S7B). Notably, at low Cl^- concentrations (2.8 mM NaCl), the wild type exhibited a higher pK_a
199 than the E292A mutant (8.0 and 6.1, respectively). However, at 500 mM NaCl, the pK_a of the E292A
200 mutant and wild type were comparable (9.0 and 8.9, respectively; Fig. 3A, B). These results suggest
201 that Cl^-, rather than Glu292, serves as the counterion in the dark state of Antho2a, while Glu292
202 facilitates the protonation of the Schiff base by the Cl^- counterion.
203
204 *(d) Binding affinity of Cl^- to wild type Antho2a and the E292A mutant*
205 To evaluate the Cl^- binding affinities of both wild type Antho2a and the E292A mutant, we measured
206 changes in their absorption spectra by gradually increasing Cl^- concentrations at pH 6.5 and estimated
207 the Cl^- dissociation coefficients (K_d). The relative absorbance in the visible region increased with
208 higher Cl^- concentrations both in the wild type and the E292A mutant (Fig. S9A, B). By fitting the
209 Hill equation to the experimental data (Fig. 3C), the dissociation constants (K_d) of Cl^- were
210 determined to be 0.079 ± 0.010 mM for the wild type Antho2a and 12.7 ± 0.519 mM for the E292A
211 mutant. This significant increase in the K_d value for the E292A mutant suggests that the Cl^- binding
212 affinity is considerably reduced due to the mutation. Consequently, we suggest that while Glu292 does
213 not act as a direct counterion, it plays a crucial role in facilitating Cl^- binding to Antho2a.
214
215 **Structural modelling and QM/MM calculations of the dark state of Antho2a**
216 To gain a deeper understanding of the environment surrounding the retinylidene Schiff base in the
217 dark state of Antho2a, we performed QM/MM-based structural modelling of both the wild type
218 Antho2a (with Glu292 either neutral or negatively charged) and the E292A mutant. The QM/MM
219 geometry optimization positioned the Cl^- ion close to the Schiff base (~3Å) and near Glu292 (~4.7Å),
220 with Glu292 itself located in proximity to the Schiff base (~3.3Å) (Fig. 4B). The chloride ion is also
221 coordinated by two water molecules and the backbone of Cys187 which is part of a conserved

222 disulfide bridge (Fig. S2). The retinylidene Schiff base region also includes polar (Ser186, Tyr91) and
223 non-polar (Ala94, Leu113) residues (Fig. 4). To validate these models, we calculated the QM/MM
224 vertical excitation energies of the ground state geometries (Table S1).
225 For wild type Antho2a with a protonated neutral Glu292, the calculated λ_{max} using the CAM-
226 B3LYP/cc-pVTZ level of theory was 503 nm (Fig. 4B), in good agreement with the experimentally
227 observed value (503 nm; Fig. 2A). In contrast, the λ_{max} calculated with a deprotonated negatively
228 charged Glu292 was blue-shifted to 415 nm (Fig. 4C), deviating significantly from the experimental
229 value. Finally, the calculated λ_{max} for the E292A mutant was 499 nm (Fig. 4D), also in agreement with
230 the experimental value (505 nm). To further substantiate these findings, we recalculated the excitation
231 energies using the RI-ADC(2)/cc-pVTZ method. Although these λ_{max} values are blue-shifted compared
232 to those calculated with the CAM-B3LYP method, they followed a similar trend. Both these
233 computational methods have previously been employed to accurately calculate the excitation energies
234 of rhodopsins (Church et al., 2021). These results strongly suggest that in the dark state of Antho2a,
235 Glu292 is protonated and neutral at pH 6.5, and therefore, it does not function as the counterion.
236
237 **Effect of the Glu292 mutation on the function of the photoproduct**
238 The spectroscopy data indicate that Glu292 is involved in stabilizing the protonated Schiff base by
239 facilitating Cl^- binding in the dark state and also serves as a counterion in the photoproduct. This
240 suggests that Glu292 significantly contributes to the visible light absorption of Antho2a. To explore
241 additional roles of Glu292 in Antho2a, we measured the light-induced Ca^{2+} response in cultured cells
242 expressing wild type Antho2a or the E292A mutant. Notably, cells expressing wild type Antho2a
243 showed a ~30-fold increase in Ca^{2+} levels upon light irradiation (Fig. 5, solid black circles), whereas
244 cells expressing the Antho2a E292A mutant showed a smaller Ca^{2+} elevation (< 5-fold increase) (Fig.
245 5, red open circles). This indicates that the peak Ca^{2+} response in cells expressing wild type Antho2a
246 was approximately nine times greater than in cells expressing the E292A mutant. This result, along
247 with the crucial role of Glu292 in Cl^- binding in the dark state and as a counterion in the photoproduct,
248 suggests that Glu292 plays also a role in G protein activation.

Cl^--dependent changes in the absorption spectra of the dark states of Antho2c and Antho2e

We tested whether Cl^- concentration affects the pK_a of the Schiff base in another visible light-sensitive opsin, Antho2c (λ_{max} = 450 nm, Fig. 1C). The pH-dependent equilibrium between UV- and visible-light absorbing forms was clearly observed at 0 mM or 0.093 mM NaCl, but not at 9.3 mM NaCl, where Antho2c stably absorbed visible light across the measured pH range (pH 4.8 to 7.2, Fig. 6A–C). Also, the ratio of UV to visible-light absorption increased with higher Cl^- concentrations at pH 6.5 (Fig. 6D). These results demonstrate that Cl^- serves as a counterion in the dark state of Antho2c, as it does in Antho2a. In contrast, wild type Antho2e continues to absorb UV light even at 1 M NaCl (Fig. 6E). Notably, Antho2e has an arginine at position 113, which corresponds to the counterion position in vertebrate visual opsins (Fig. S2). When this arginine is mutated to alanine (R113A), the mutant becomes sensitive to visible light (λ_{max} = ~420 nm) in the presence of Cl^- (Fig. 6F), suggesting that Cl^- can serve as the counterion in the R113A mutant.

Discussion

In this study, we reveal for the first time the spectral properties of opsins in the ASO-II group from the coral *Acropora tenuis*, showing that their sensitivity spans from UV to visible light. Opsins in this group have a highly conserved Glu292 residue near the Schiff base, which can potentially stabilize the proton on the Schiff base. Indeed, our results show that the pK_a of the protonated Schiff base in the photoproduct (λ_{max} = 476 nm) of Antho2a is altered when Glu292 is substituted with alanine (Fig. 2A, B; Fig. S4), suggesting that Glu292 serves as the counterion of the photoproduct. Conversely, the dark state of Antho2a (λ_{max} = 503 nm) exhibits robust visible light absorption only in the presence of Cl^- at physiological pH, and the pK_a of the protonated Schiff base changes with Cl^- concentration in both wild type Antho2a and the E292A mutant. Furthermore, the pK_a for wild type and the E292A mutant are comparable in the presence of sufficient Cl^- (500 mM NaCl, Fig. 3A, B), supporting the conclusion that Cl^-, and not Glu292, acts as the counterion of the dark state of *A. tenuis* Antho2a. We

275 found that the type of halide anions in the solution has a small but noticeable effect on the λ_{max} values
276 of the dark state of Antho2a. This is consistent with the effect observed in a counterion-less mutant of
277 bovine rhodopsin, in which halide ions serve as surrogate counterions (Nathans, 1990; Sakmar et al.,
278 1991). Similarly, our results align with earlier observations that the λ_{max} of a retinylidene Schiff base in
279 solution increases with the ionic radius of halides acting as hydrogen bond acceptors (i.e., $I^- > Br^- >$
280 Cl^-) (Blatz et al., 1972). In contrast, the λ_{max} of halorhodopsin from *Natronobacterium pharaonic* does
281 not clearly correlate with halide ionic radius (Scharf and Engelhard, 1994), as the halide ion in this
282 case is not a hydrogen-bonding acceptor of the protonated Schiff base (Kouyama et al., 2010; Mizuno
283 et al., 2018). Altogether, these findings support our hypothesis that in Antho2a, a solute halide ion
284 forms a hydrogen bond with the Schiff base, thereby serving as the counterion in the dark state.
285 Moreover, QM/MM calculations for the dark state of Antho2a suggest that Glu292 is protonated and
286 neutral, further supporting the hypothesis that Glu292 does not serve as the counterion in the dark
287 state. However, unlike dark state, Cl^- has little to no effect on the visible light absorption of the
288 photoproduct (Fig. S5). Therefore, we conclude that Cl^- and Glu292, respectively, act as counterions
289 for the protonated Schiff base of the dark state and photoproduct of Antho2a. This represents a unique
290 example of counterion switching from exogeneous anion to a specific amino acid residue upon light
291 irradiation (Fig. S10).

292 Our spectroscopic data also showed that the other visual light sensitive opsin, Antho2c, exhibited
293 the Cl^- dependency on the Schiff base pK_a of the dark state, which suggesting that opsins in the ASO-
294 II group may share a spectral tuning mechanism based on the Cl^- counterion. Interestingly, Antho2e
295 had an arginine at position 113 and when it was mutated to alanine (R113A), the mutant showed
296 sensitivity to visible light in the presence of Cl^- (Fig. 6F). We hypothesize that the positive charge of
297 Arg113 disturbs interaction between the Cl^- and the protonated Schiff base or that it completely
298 inhibits Cl^- binding, rendering Antho2e UV-sensitive.

299 It is noteworthy that although Cl^- has been reported to serve as a surrogate counterion in
300 "counterion-less" mutants of animal opsins (such as E113Q in bovine rhodopsin and E181Q in
301 retinochrome) (Nathans, 1990; Sakmar et al., 1991; Terakita et al., 2000), Antho2a is, to our

knowledge, the first example in a wild type animal opsin that employs Cl^- as a counterion. Interestingly, within the microbial rhodopsin family, heliorhodopsin (TaHeR) incorporates a Cl^- into the Schiff base region under high Cl^- concentrations at pH 4.5. This Cl^- stabilizes the protonated retinal Schiff base when its primary counterion, E108, is neutralized (Besaw et al., 2022). The observed 18 nm red shift at low pH is consistent with E108 protonation. The TaHeR E108A mutant shows the same λ_{max} under high Cl^- concentrations, further supporting the role of Cl^- as a counterion. At pH 8, the Schiff base proton is stabilized by the negatively charged E108 (Shihoya et al., 2019).

The E292A mutation in Antho2a drastically decreases the Cl^- binding affinity in the dark state at pH 6.5 (K_d: Antho2a WT = 0.079 mM, Antho2a E292A = 12.7 mM). Based on these results, supported by our QM/MM calculations of the dark state, we hypothesize that protonated Glu292 not only serves as a counterion of the photoproduct but also constitutes part of the Cl^- binding site in the dark state of Antho2a. In Cl^--pumping microbial rhodopsins, where Cl^- serves as a counterion, the Cl^- binding site near the Schiff base is typically formed by hydrogen-bonding network between Cl^-, the protonated Schiff base, and key amino acids such as serine, threonine and glutamic/aspartic acid, and water molecules (Besaw et al., 2020; Hosaka et al., 2016; Kolbe et al., 2000). Additionally, the bovine rhodopsin double mutant E113Q/A292E exhibits a higher sensitivity to hydroxylamine than the wild type, indicating instability of the Schiff base and increased solvent accessibility (Tsutsui and Shichida, 2010). These observations suggest that Glu292 in Antho2a may also facilitate the accessibility of Cl^- ions to the Schiff base environment. To determine the precise nature of the Cl^- binding site and clarify the roles of Glu292 and other residues in the Cl^--dependent counterion system of Antho2a, detailed spectroscopic and structural experiments will be necessary.

We also found that cells expressing the Antho2a E292A mutant show a lower Ca^{2+} elevation upon light stimulation compared to the wild type (Fig. 5). The relative expression level of the E292A mutant of Antho2a was approximately 0.81 of the wild type (set as 1), as determined by comparing absorbances at λ_{max} for both pigments expressed and purified under identical conditions (Fig. S11A). Additionally, the fraction of protonated pigment relative to the wild type (set as 1 at pH 6.5) was estimated to be 0.94 for the E292A mutant at pH 6.5, and 0.99 and 0.84 for the wild type and the

329 E292A mutant at pH 7.0, respectively (Fig. 3A and B). Since pH 7.0 corresponds to the conditions
330 used in the live cell Ca^{2+} assays, the effective amount of protonated pigment for the E292A mutant was
331 approximately 73% of the wild type. Nevertheless, even after normalization for these differences, the
332 Ca^{2+} response amplitude of the E292A mutant remained significantly lower (~ 17% of wild type,
333 compared to the observed 12% prior to normalization; Fig. 5 and Fig. S11B). These observations
334 suggest that Glu292 serves not only as a counterion in the photoproduct but also plays an allosteric
335 role in influencing G protein activation. It has been reported that the introduction of Glu or Asp at
336 position 292 can affect various molecular properties of opsins. For instance, the A292E mutation in
337 human rhodopsin has been shown to result in constitutively active apoproteins, leading to congenital
338 night blindness (Dryja et al., 1993; Jin et al., 2003). These data suggest that Glu292 has the potential
339 to influence functional properties, such as G protein activation. Several studies have reported that the
340 counterion can affect diverse properties of opsins beyond their absorption spectra. For instance, in
341 bovine rhodopsin, Glu113 is involved not only in visible light absorption in the dark state but also in
342 the efficient activation of G proteins by the photoproduct (Terakita et al., 2004). It has been suggested
343 that these pleiotropic functions of the counterion have been achieved through evolutionary
344 modifications of the protein structure once the counterion was acquired (Terakita et al., 2004). This
345 concept may similarly apply to Antho2a.
346 One of the notable features of the opsins in the ASO-II group that use Cl^- as a counterion is the
347 relatively low pK_a of the Schiff base (e.g., ~9.0 for Antho2a in the dark state, Fig. 3A) compared to
348 other animal opsins with a "regular" amino acid counterion (e.g., >16 for bovine rhodopsin, with
349 Glu113 as a counterion (Steinberg et al., 1993) or 11 for jumping spider Rh1, with Glu181 as a
350 counterion (Nagata et al., 2019)). We hypothesize that opsins in the ASO-II group, with lower Schiff
351 base pK_a, may change their spectral sensitivity and G protein activation profile within the
352 physiological pH range of corals. For instance, these opsins could exhibit decreased sensitivity to
353 visible and increased sensitivity to UV light under alkaline pH conditions. The extra- and intracellular
354 pH environments in symbiotic cnidarians such as corals are spatially and temporally variable due to
355 the photosynthesis of symbiotic algae (Barott et al., 2017). For example, pH values in the cytosol of

356 algae-hosting cells (a group of endodermal cells with algal occupancy) in corals reportedly increase by
357 approximately 0.5 pH units upon light treatment (Venn et al., 2009). The pH values in the
358 gastrovascular cavity (coelenteron), which is in contact with endodermal cells, range from 6.6 to 8.5
359 (Agostini et al., 2012; Al-Horani et al., 2003; Cai et al., 2016) and increase in the presence of light,
360 presumably due to the consumption of CO_2 by photosynthesis (Barott et al., 2017). Additionally,
361 alkalinization in extracellular region of calcifying cells reportedly increases ~1.0 pH units from dark to
362 light conditions reaching levels above pH 9.0 (Al-Horani et al., 2003). These pH changes, generally an
363 increase due to photosynthetic activity, may result in variable light sensitivity of the "low pK_a" opsins
364 in the ASO-II group. Recent studies have reported that members of the ASO-II group may be
365 associated with the symbiotic relationship between host anthozoans and symbiotic algae. For example,
366 using the symbiotic sea anemone *Exaiptasia diaphana*, Gornik et al. (2021) showed that the mRNA
367 levels of several opsins in the ASO-II group were higher in symbiotic adults than in apo-symbiotic
368 ones (Gornik et al., 2020). In sea anemone, it has also been reported that behavioral responses to light
369 differ between symbiotic and apo-symbiotic individuals (Foo et al., 2020; Kishimoto et al., 2023),
370 with these responses potentially being driven by the activation of ASO-II opsins that are up-regulated
371 in the presence of symbiotic algae. Moreover, single-cell RNA-seq analysis in the reef-building coral
372 *Stylophora pistillata* has revealed that an opsin belonging to the ASO-II group is specifically
373 expressed in algae-hosting cells (a group of endodermal cells with 50% algal occupancy) (Levy et al.,
374 2021). Although further studies are needed, we suggest that the unique use of Cl^- as the counterion in
375 opsins of ASO-II group, rather than a negatively charged amino acid, may be associated to their pH-
376 sensitive light response and, ultimately, to their role in photosynthesis-related functions in symbiotic
377 cnidarians.

378 It is widely accepted that opsins have evolved from a non-opsin GPCR (Feuda et al., 2012). Our
379 finding of the native chloride counterion in opsins shows a possibility that in the first stage of the
380 evolutionary process, the "primitive" opsins having Lys296 but no counterion residue could absorb not
381 only UV light but also a wide range of wavelengths that extends into the visible region by embracing
382 chloride ions. Namely, the chloride counterion system might have been a preliminary step in the

383 evolution of amino acid counterions in animal opsins. Further empirical and bioinformatic studies are
384 required for disentangling the evolutionary trajectories of the Schiff base – counterion system,
385 including the chloride counterion.
386

387 # Materials and Methods

388 **Experimental design**

389 We first identified and cloned opsins from a reef-building coral, *Acropora tenuis*, and then expressed
390 opsins belong to the ASO-II group in mammalian cultured cells. We performed spectroscopic
391 measurements of purified pigments of the opsins in different pH and Cl^- conditions to identify their
392 effects on the acid dissociation constant of the protonated Schiff base of the opsins, leading to the
393 determination of the counterion. Computational modelling and QM/MM calculations were also
394 conducted to elucidate the retinylidene Schiff base environment in the dark state of Antho2a. Light-
395 evoked Ca^{2+} responses were assessed by aequorin-based bioluminescent reporter assay to evaluate the
396 G protein activation of Antho2a.
397

398 **Identification of *Acropora tenuis* opsins and phylogenetic tree inference**

399 *Acropora tenuis* (Dana, 1846) is a common reef-building coral distributed throughout the Indo-Pacific
400 Ocean. Candidate sequences of *A. tenuis* opsins were identified by homology search against public
401 genome and transcriptome datasets (Shinzato et al., 2020; Voolstra et al., 2015) and their phylogenetic
402 relationships to known opsins were inferred by subsequent phylogenetic tree reconstruction. We first
403 conducted BLASTP and TBLASTN searches with an E-value cut-off of 10^{-10} using *Acropora palmata*
404 Acropsin 1–3 (JQ966100 – JQ966102), two *Nematostella vectensis* opsins (BR000676 – BR000677),
405 human rhodopsin (NM_000539), and squid rhodopsin (X70498) as queries. We aligned the collected
406 opsin homologs and excluded sequences which did not contain a retinal-binding lysine residue
407 (Lys296) in the seventh transmembrane helix. We modified the fragmented sequences by reference to
408 the genome sequence of *A. tenuis* and opsin sequences of other *Acropora* species (*A. palmata* or *A.*

409 *millepora*). The candidate sequences of *A. tenuis* opsins were combined with the representative opsin
410 sequences. The final sequence set was aligned using MAFFT (Katoh and Standley, 2013) and trimmed
411 by TrimAl (Capella-Gutiérrez et al., 2009) with the "*gappyout*" function. The ML tree was
412 reconstructed using RAxML-NG v1.1.0 (Kozlov et al., 2019) assuming the LG + G4 model of protein
413 evolution, which was selected by ModelTest-NG v0.2.0 (Darriba et al., 2020). The ML branch
414 supports were estimated with 1000 bootstrap replicates.
415
416 **Sample collection, total RNA extraction, and cDNA synthesis**
417 Colonies of *A. tenuis* were collected from < 3 m depth on the fringing reef on Sesoko Island, Okinawa
418 (N26°37.58′, E127°52.01′) and were maintained in flow-through aquaria at Sesoko Station (Tropical
419 Biosphere Research Center, University of Ryukyus, Okinawa, Japan). Four days after spawning,
420 motile larvae and small branches of adult colonies were preserved in RNAlater® Stabilization
421 Solution (Thermo Fisher Scientific, MA, USA). Total RNAs were extracted from the larval and adult
422 samples using TRIzol reagent (Thermo Fisher Scientific) or Sepasol-RNA I Super G (nacalai tesque,
423 Kyoto, Japan) and purified using Qiagen RNeasy mini kits (Qiagen, Hilden, Germany) following the
424 manufacturer's protocol. cDNAs were synthesized from the total RNA by reverse transcription using
425 High-Capacity cDNA Reverse Transcription kits (Thermo Fisher Scientific).
426
427 **Expression and purification of *Acropora tenuis* opsins**
428 The coding regions of *A. tenuis* opsins were amplified by PCR with gene-specific primers and were
429 tagged with the epitope sequence of the anti-bovine rhodopsin antibody rho 1D4 (ETSQVAPA) at their
430 C-termini. Site-directed mutants were produced by overlap extension PCR using PrimeSTAR Max
431 DNA Polymerase (TAKARA, Shiga, Japan) with site-specific primers and were also tagged with the
432 1D4 epitope sequence. The tagged cDNAs were inserted into the pUSRα vector (Kayada et al., 1995)
433 digested with HindIII and EcoRI or the pMT vector (Ridge and Abdulaev, 2000) digested with EcoRI
434 and NotI using In-Fusion HD cloning kit (TAKARA). The plasmids (15 μg per 100 mm culture dish)
435 were transfected into COS-1 cells using the polyethyleneimine (PEI) transfection method as described

436 previously (Obayashi et al., 2025; Sinha et al., 2014). The transfected cells were maintained for 24 h
437 after transfection at 37°C under 5% CO_2 and then 11-*cis* retinal was added to the medium (1 μL of 4
438 mM 11-*cis* retinal to 100 mm culture dish) following 25°C or 30°C incubation for another 24 h in the
439 dark before collecting the cells. The reconstituted pigments were extracted from the cell membranes
440 with 1% dodecyl β-D-maltoside (DDM, Dojindo, Kumamoto, Japan), 50 mM HEPES, and 140 mM
441 NaCl (pH 6.5). The solubilized samples were mixed with 1D4-condjugated agarose beads overnight,
442 and the mixture was transferred into Bio-Spin columns (Bio-Rad, Hercules, CA, USA) and washed in
443 the buffer containing 0.02% DDM, 50 mM HEPES, and 140 mM NaCl (pH 6.5, buffer A). The
444 purified pigments were eluted with buffer A containing 0.5 ~ 1 mg/mL 1D4 peptide (custom peptide
445 synthesis by GenScript Japan Inc., Tokyo, Japan). To obtain pigments in solutions of various anions
446 (SO_4^{2-}, Br^-, and I^-) other than Cl^-, samples were prepared as described above and in the final step the
447 mixture of solubilized samples and 1D4-agarose beads was washed with buffer A followed by the
448 additional wash with buffers including different sodium salts of anions (0.02% DDM, each of 70 mM
449 Na_2SO_4, 140 mM NaBr, or 140 mM NaI, and 50 mM HEPES). Then the pigments were eluted with the
450 buffer including the appropriate sodium salt of anion containing 0.5 ~ 1 mg/mL 1D4 peptide.
451 Alternatively, for some pigments that were unstable under the absence of Cl^-, we quickly removed Cl^-
452 by gel-filtration chromatography on PD MiniTrap desalting columns with Sephadex G-25 resin
453 (Cytiva, Marlborough, MA, USA). The columns were first equilibrated with the buffer including
454 0.02% DDM, 70 mM Na_2SO_4, and 50 mM HEPES, 500 μL of samples were loaded onto the columns
455 and eluted with the buffer. We collected 800 μL fractions and used them for subsequent spectroscopic
456 analyses.
457
458 **UV-visible spectroscopy**
459 Spectroscopic measurements were performed at 0°C using a V-750 UV-visible spectrophotometer
460 (JASCO Corporation, Tokyo, Japan). The pH of the samples was adjusted with 100 mM CAPS
461 including NaOH for alkaline conditions and 500 mM NaH_2PO_4 for acidic conditions. pH values were
462 measured using a pH meter (B-211; HORIBA, Kyoto, Japan) immediately after each spectroscopic

463 measurement. The concentration of Cl^- in the samples was adjusted by addition of different
464 concentrations of NaCl solutions which were prepared in 70 mM Na_2SO_4 buffer (see above). A 100-W
465 halogen lamp was equipped on the spectrophotometer and used to illuminate samples with a set of
466 optical interference filters (420 nm or 500 nm, Toshiba) and cut-off filters (O-55 or O-56, AGC
467 Techno Glass Co., Shizuoka, Japan). Absorption spectra of some UV-absorbing pigments were
468 recorded using the V-750 UV-visible spectrophotometer, equipped with a 300-W xenon lamp (MAX-
469 350; Asahi Spectra Co., Tokyo, Japan) that was used for illumination of samples in combination with a
470 UV-transmitting filter (UTVAF-50S-36U, SIGMA KOKI, Tokyo, Japan).
471
472 **HPLC analysis**
473 An HPLC analysis was carried out to analyze the conformations of retinal present in the purified
474 pigments as described previously (Terakita et al., 1989), with some modifications. Briefly, 100 μL of
475 purified pigments were mixed with 210 μL of cold 90% methanol which was stored in −20°C and 30
476 μL of 1 M hydroxylamine to convert retinal chromophore in a sample into retinal oxime. The retinal
477 oxime was extracted with 700 μL of *n*-hexane. 200 μL of the extract were injected into a YMC-Pack
478 SIL column (particle size 3 μm, 150 × 6.0 mm) and eluted with *n*-hexane containing 15% (v/v) ethyl
479 acetate and 0.15% (v/v) ethanol at a flow rate of 1 mL/min.
480
481 **Bioluminescent reporter assays for Ca^{2+} measurements in cultured cells**
482 Ca^{2+} levels in opsin-expressing cultured cells were assessed by an aequorin-based luminescent assay
483 as described previously (Koyanagi et al., 2022). Briefly, the plasmid containing open reading frames
484 of each opsin was transfected into HEK293S cells in 35 mm dishes by the PEI method with the
485 aequorin plasmid obtained by introducing a reverse mutation A119D into the plasmid
486 [pcDNA3.1+/mit-2mutAEQ] (Addgene no. 45539) (de la Fuente et al., 2012). The transfected
487 HEK293S cells were incubated for ~24 hours at 37°C under 5% CO_2 with the addition of 0.2 μM/dish
488 of 11-*cis* retinal 4 ~ 5 hours after the transfection. Before the luminescence measurements, the culture
489 medium was replaced with a medium containing Coelenterazine *h* (pH 7.0), and the cells were

incubated to equilibrate with the media at 25°C for at least 2 hours. Dishes of cells were then stimulated with light and luminescence values were recorded using GloMax 20/20n Luminometer (Promega). A green (495 nm) LED light (color: "Cyan", Ex-DHC; BioTools Inc., Gunma, Japan) and arrayed LEDs on a board with spectral emission peaks at 390 nm and 510 nm (SPL-25-CC; REVOX Inc., Kanagawa, Japan) were used as light sources.

Computational modelling and QM/MM calculations

The three-dimensional structure of Antho2a was predicted from the primary amino acid sequence using AlphaFold2 (Jumper et al., 2021). The 11-*cis* retinal chromophore linked to the protonated Schiff base was incorporated into the AlphaFold model using as a template the high-resolution structure of bovine rhodopsin solved by time-resolved serial femtosecond X-ray crystallography (Gruhl et al., 2023). A Cl^- anion was initially placed in close proximity to the retinal protonated Schiff base, as observed in the microbial chloride-pump halorhodopsin (Mous et al., 2022). Water molecules were added using HomolWat (Mayol et al., 2020). We determined the pK_a values of the titratable amino acid residues at pH 6.5 using the PROPKA program (Olsson et al., 2011; Søndergaard et al., 2011) and subsequently, the protein was protonated using the tleap program in the AMBER software package (Case et al., 2016). The geometry of this initial model was first relaxed by molecular mechanics energy minimization with the Amber ff14SB force field (Maier et al., 2015) using steepest descent for 10,000 steps before switching to a conjugate gradient minimiser for an additional 10,000 steps. During energy minimization, a positional restraint of 10 kcal $mol^{-1}Å^{-2}$ was applied to all atoms, including hydrogens. The SHAKE algorithm (Ryckaert et al., 1977) was used to constrain the motion of bonds involving hydrogen. Finally, the geometry of the system was optimized using hybrid quantum mechanics/molecular mechanics (QM/MM) calculations without considering any external environment and with the backbone of the protein frozen (Mroginski et al., 2021; Senn and Thiel, 2009). The QM part consists of the retinal chromophore linked to the lysine sidechain cut between the Cδ and Cε atoms forming the protonated Schiff base, along with Cl^-, Glu292 and Ser186. The retinal-binding pocket also contains predicted water molecules (modelled based on homologous GPCR

structures) close to the Schiff base and the chloride ion which were not included in the QM region. The hydrogen link atom (HLA) scheme was used at the QM/MM boundary. The QM part was treated using the BP86-D3 (BJ) functional (Becke, 1988; Grimme et al., 2011) in conjunction with the cc-pVDZ basis set (Dunning, 1989) and the def2/J auxiliary basis set for the resolution of identity (RI) (Weigend, 2008). The Chain of Spheres exchange (COSX) algorithm was utilized in combination with the resolution of identity for the Coulomb term (RI-J). The rest of the protein was treated with the Amber ff14SB force field. Water molecules were treated with the TIP3P model (Jorgensen et al., 1983). The QM/MM calculations were performed using the quantum chemistry program Orca 5.0.2 (Neese, 2022) interfaced with the DL_POLY module of the ChemShell 3.7.1 software package (Metz et al., 2014; Sherwood et al., 2003). The optimized ground state geometries and partial charges were used to calculate the vertical excitation energies using the simplified time-dependent density functional theory (sTD-DFT) (Bannwarth and Grimme, 2014; Runge and Gross, 1984) at the CAM-B3LYP/cc-pVTZ level of theory (Dunning, 1989; Yanai et al., 2004) using the Orca program. The excitation energies were also calculated using the RI-ADC(2) method (Hättig, 2005) with frozen core orbitals and the cc-pVTZ basis set in association with the corresponding auxiliary basis by utilizing the Turbomole 7.5.1 program package (Furche et al., 2014). The three-dimensional models were visualized using the molecular graphics program PyMOL 2.5.5.

Acknowledgements

We thank Dr. Robert S. Molday (University of British Columbia) for kindly supplying rho 1D4-producing hybridoma. We thank Dr. Masayuki Hatta (Ochanomizu University) for coral sampling. We are also grateful to Dr. Hisao Tsukamoto for technical guidance on the transfection of COS-1 cells. This work was supported by the Japanese Ministry of Education, Culture, Sports, Science and Technology Grants-in-Aid for Scientific Research 23H02516 (to AT), 22H02663 (to MK) and JP20J01841 (YS); and Japan Science and Technology Agency (JST) Core Research for Evolutional Science and Technology (CREST) Grant JPMJCR1753 (to AT). YS was supported by Grant-in-Aid for JSPS Fellows. This work has also been supported by the Swiss National Science Foundation (project grant 192780 to XD) and by the European Union's Horizon 2020 research and innovation programme (grant agreement 951644 to GFXS and Marie Skłodowska-Curie grant agreement 884104 (PSI-FELLOW-III-3i) to SS). We finally thank the members of the High-Performance Computing and Emerging Technologies (HPCE) group at the Paul Scherrer Institute for technical support and assistance with high-performance computing.

Author contributions: YS, MK, and AT conceptualized the study; YS, MK, GFXS, XD, and AT designed the study; YS, TS, YK, and MI performed the experiments and analyses; SS and XD performed the computational modelling; YS and AT wrote the original draft with inputs from SS and XD; All authors reviewed the manuscript and gave final approval for the manuscript.

Competing interests: The authors declare that they have no competing interests.

Data and materials availability: The cDNA sequences of Acropora tenuis opsins in this paper are available in GenBank: eight Cnidopsins (accession no. LC844924–LC844931), seven opsins in the ASO-II group (accession no. LC844932–LC844938), and one opsin in the ASO-I group (accession no. LC844939). The structural models of wild type Antho2a with a neutral or charged Glu292 and the

Antho2a E292A mutant are available in Zenodo (10.5281/zenodo.15064942). All data needed to evaluate the conclusion in this paper are present in the paper and the Supplementary Materials. Additional data related to this paper may be requested from the authors.

References

Agostini S, Suzuki Y, Higuchi T, Casareto BE, Yoshinaga K, Nakano Y, Fujimura H. 2012. Biological and chemical characteristics of the coral gastric cavity. *Coral Reefs* **31**:147–156. doi:10.1007/s00338-011-0831-6

Al-Horani FA, Al-Moghrabi SM, de Beer D. 2003. The mechanism of calcification and its relation to photosynthesis and respiration in the scleractinian coral Galaxea fascicularis. *Mar Biol* **142**:419–426. doi:10.1007/s00227-002-0981-8

Bannwarth C, Grimme S. 2014. A simplified time-dependent density functional theory approach for electronic ultraviolet and circular dichroism spectra of very large molecules. *Computational and Theoretical Chemistry* **1040–1041**:45–53. doi:10.1016/j.comptc.2014.02.023

Barott KL, Barron ME, Tresguerres M. 2017. Identification of a molecular pH sensor in coral. *Proc R Soc Lond B Biol Sci* **284**:20171769. doi:10.1098/rspb.2017.1769

Becke AD. 1988. Density-functional exchange-energy approximation with correct asymptotic behavior. *Phys Rev A* **38**:3098–3100. doi:10.1103/PhysRevA.38.3098

Besaw JE, Ou W-L, Morizumi T, Eger BT, Sanchez Vasquez JD, Chu JHY, Harris A, Brown LS, Miller RJD, Ernst OP. 2020. The crystal structures of a chloride-pumping microbial rhodopsin and its proton-pumping mutant illuminate proton transfer determinants. *J Biol Chem* **295**:14793–14804. doi:10.1074/jbc.RA120.014118

Besaw JE, Reichenwallner J, De Guzman P, Tucs A, Kuo A, Morizumi T, Tsuda K, Sljoka A, Miller RJD, Ernst OP. 2022. Low pH structure of heliorhodopsin reveals chloride binding site and intramolecular signaling pathway. *Sci Rep* **12**:13955. doi:10.1038/s41598-022-17716-9

Blatz PE, Mohler JH, Navangul HV. 1972. Anion-induced wavelength regulation of absorption maxima of Schiff bases of retinal. *Biochemistry* **11**:848–855. doi:10.1021/bi00755a026

Cai W-J, Ma Y, Hopkinson BM, Grottoli AG, Warner ME, Ding Q, Hu X, Yuan X, Schoepf V, Xu H, Han C, Melman TF, Hoadley KD, Pettay DT, Matsui Y, Baumann JH, Levas S, Ying Y, Wang Y. 2016. Microelectrode characterization of coral daytime interior pH and carbonate chemistry. *Nat Commun* **7**:11144. doi:10.1038/ncomms11144

Capella-Gutiérrez S, Silla-Martínez JM, Gabaldón T. 2009. trimAl: a tool for automated alignment trimming in large-scale phylogenetic analyses. *Bioinformatics* **25**:1972–1973. doi:10.1093/bioinformatics/btp348

Case DA, Betz RM, Cerutti DS, Cheatham TE III, Darden TA, Duke RE, Giese TJ, Gohlke H, Goetz AW, Homeyer N, Izadi S, Janowski P, Kaus J, Kovalenko A, Lee TS, LeGrand S, Li P, Lin C, Luchko T, Luo R, Madej B, Mermelstein D, Merz KM, Monard G, Nguyen H, Nguyen HT, Omelyan I, Onufriev A, Roe DR, Roitberg A, Sagui C, Simmerling CL, Botello-Smith WM, Swails J, Walker RC, Wang J, Wolf RM, Wu X, Xiaoand L, Kollman PA. 2016. AMBER 2016. San Francisco: University of California.

599 Church JR, Olsen JMH, Schapiro I. 2021. The impact of retinal configuration on the protein-
600 chromophore interactions in bistable jumping spider rhodopsin-1. *Molecules* **27**:71.
601 doi:10.3390/molecules27010071
602 Darriba D, Posada D, Kozlov AM, Stamatakis A, Morel B, Flouri T. 2020. ModelTest-NG: a new and
603 scalable tool for the selection of DNA and protein evolutionary models. *Mol Biol Evol*
604 **37**:291–294. doi:10.1093/molbev/msz189
605 de la Fuente S, Fonteriz RI, de la Cruz PJ, Montero M, Alvarez J. 2012. Mitochondrial free [Ca^{2+}]
606 dynamics measured with a novel low-Ca^{2+} affinity aequorin probe. *Biochem J* **445**:371–376.
607 doi:10.1042/BJ20120423
608 Dryja TP, Berson EL, Rao VR, Oprian DD. 1993. Heterozygous missense mutation in the rhodopsin
609 gene as a cause of congenital stationary night blindness. *Nat Genet* **4**:280–283.
610 doi:10.1038/ng0793-280
611 Dunning TH Jr. 1989. Gaussian basis sets for use in correlated molecular calculations. I. The atoms
612 boron through neon and hydrogen. *J Chem Phys* **90**:1007–1023. doi:10.1063/1.456153
613 Feuda R, Hamilton SC, Mclnerney JO, Pisani D. 2012. Metazoan opsin evolution reveals a simple
614 route to animal vision. *Proc Natl Acad Sci U S A* **109**:18868–18872.
615 doi:10.1073/pnas.1305990110
616 Foo SA, Liddell L, Grossman A, Caldeira K. 2020. Photo-movement in the sea anemone Aiptasia
617 influenced by light quality and symbiotic association. *Coral Reefs* **39**:47–54.
618 doi:10.1007/s00338-019-01866-w
619 Furche F, Ahlrichs R, Hättig C, Klopper W, Sierka M, Weigend F. 2014. Turbomole. *Wiley Interdiscip*
620 *Rev Comput Mol Sci* **4**:91–100. doi:10.1002/wcms.1162
621 Gerrard E, Mutt E, Nagata T, Koyanagi M, Flock T, Lesca E, Schertler GFX, Terakita A, Deupi X,
622 Lucas RJ. 2018. Convergent evolution of tertiary structure in rhodopsin visual proteins from
623 vertebrates and box jellyfish. *Proc Natl Acad Sci U S A* **115**:6201–6206.
624 doi:10.1073/pnas.1721333115
625 Gornik SG, Bergheim BG, Morel B, Stamatakis A, Foulkes NS, Guse A. 2020. Photoreceptor
626 diversification accompanies the evolution of Anthozoa. *Mol Biol Evol* **38**:1744–1760.
627 doi:10.1093/molbev/msaa304
628 Grimme S, Ehrlich S, Goerigk L. 2011. Effect of the damping function in dispersion corrected density
629 functional theory. *J Comput Chem* **32**:1456–1465. doi:10.1002/jcc.21759
630 Gruhl T, Weinert T, Rodrigues MJ, Milne CJ, Ortolani G, Nass K, Nango E, Sen S, Johnson PJM,
631 Cirelli C, Furrer A, Mous S, Skopintsev P, James D, Dworkowski F, Båth P, Kekilli D, Ozerov
632 D, Tanaka R, Glover H, Bacellar C, Brünle S, Casadei CM, Diethelm AD, Gashi D, Gotthard
633 G, Guixà-González R, Joti Y, Kabanova V, Knopp G, Lesca E, Ma P, Martiel I, Mühle J,
634 Owada S, Pamula F, Sarabi D, Tejero O, Tsai C-J, Varma N, Wach A, Boutet S, Tono K, Nogly
635 P, Deupi X, Iwata S, Neutze R, Standfuss J, Schertler G, Panneels V. 2023. Ultrafast structural
636 changes direct the first molecular events of vision. *Nature* **615**:939–944. doi:10.1038/s41586-
637 023-05863-6

Hättig C. 2005. Structure optimizations for excited states with correlated second-order methods: CC2 and ADC(2) In: Jensen HJÅ, editor. Response Theory and Molecular Properties (A Tribute to Jan Linderberg and Poul Jørgensen), Advances in Quantum Chemistry. Elsevier. pp. 37–60. doi:10.1016/s0065-3276(05)50003-0

Hering L, Mayer G. 2014. Analysis of the opsin repertoire in the tardigrade *Hypsibius dujardini* provides insights into the evolution of opsin genes in Panarthropoda. *Genome Biol Evol* **6**:2380–2391. doi:10.1093/gbe/evu193

Hofmann KP, Scheerer P, Hildebrand PW, Choe HW, Park JH, Heck M, Ernst OP. 2009. A G protein-coupled receptor at work: the rhodopsin model. *Trends Biochem Sci* **34**:540–552. doi:10.1016/j.tibs.2009.07.005

Hosaka T, Yoshizawa S, Nakajima Y, Ohsawa N, Hato M, DeLong EF, Kogure K, Yokoyama S, Kimura-Someya T, Iwasaki W, Shirouzu M. 2016. Structural mechanism for light-driven transport by a new type of chloride ion pump, *Nonlabens marinus* rhodopsin-3. *J Biol Chem* **291**:17488–17495. doi:10.1074/jbc.M116.728220

Jin S, Cornwall MC, Oprian DD. 2003. Opsin activation as a cause of congenital night blindness. *Nat Neurosci* **6**:731–735. doi:10.1038/nn1070

Jorgensen WL, Chandrasekhar J, Madura JD, Impey RW, Klein ML. 1983. Comparison of simple potential functions for simulating liquid water. *J Chem Phys* **79**:926–935. doi:10.1063/1.445869

Jumper J, Evans R, Pritzel A, Green T, Figurnov M, Ronneberger O, Tunyasuvunakool K, Bates R, Žídek A, Potapenko A, Bridgland A, Meyer C, Kohl SAA, Ballard AJ, Cowie A, Romera-Paredes B, Nikolov S, Jain R, Adler J, Back T, Petersen S, Reiman D, Clancy E, Zielinski M, Steinegger M, Pacholska M, Berghammer T, Bodenstein S, Silver D, Vinyals O, Senior AW, Kavukcuoglu K, Kohli P, Hassabis D. 2021. Highly accurate protein structure prediction with AlphaFold. *Nature* **596**:583–589. doi:10.1038/s41586-021-03819-2

Katoh K, Standley DM. 2013. MAFFT multiple sequence alignment software version 7: improvements in performance and usability. *Mol Biol Evol* **30**:772–780. doi:10.1093/molbev/mst010

Kayada S, Hisatomi O, Tokunaga F. 1995. Cloning and expression of frog rhodopsin cDNA. *Comp Biochem Physiol B Biochem Mol Biol* **110**:599–604. doi:10.1016/0305-0491(94)00179-x

Kishimoto M, Gornik SG, Foulkes NS, Guse A. 2023. Negative phototaxis in the photosymbiotic sea anemone Aiptasia as a potential strategy to protect symbionts from photodamage. *Sci Rep* **13**:17857. doi:10.1038/s41598-023-44583-9

Kolbe M, Besir H, Essen LO, Oesterhelt D. 2000. Structure of the light-driven chloride pump halorhodopsin at 1.8 Å resolution. *Science* **288**:1390–1396. doi:10.1126/science.288.5470.1390

Kouyama T, Kanada S, Takeguchi Y, Narusawa A, Murakami M, Ihara K. 2010. Crystal structure of the light-driven chloride pump halorhodopsin from Natronomonas pharaonis. *J Mol Biol* **396**:564–579. doi:10.1016/j.jmb.2009.11.061

Koyanagi M, Shen B, Nagata T, Sun L, Wada S, Kamimura S, Kage-Nakadai E, Terakita A. 2022. High-performance optical control of GPCR signaling by bistable animal opsins MosOpn3 and LamPP in a molecular property-dependent manner. *Proc Natl Acad Sci U S A* **119**:e2204341119. doi:10.1073/pnas.2204341119

Koyanagi M, Takano K, Tsukamoto H, Ohtsu K, Tokunaga F, Terakita A. 2008. Jellyfish vision starts with cAMP signaling mediated by opsin-G_s cascade. *Proc Natl Acad Sci U S A* **105**:15576–15580. doi:10.1073/pnas.0806215105

Koyanagi M, Terakita A. 2014. Diversity of animal opsin-based pigments and their optogenetic potential. *Biochim Biophys Acta* **1837**:710–716. doi:10.1016/j.bbabio.2013.09.003

Kozlov AM, Darriba D, Flouri T, Morel B, Stamatakis A. 2019. RAxML-NG: a fast, scalable and user-friendly tool for maximum likelihood phylogenetic inference. *Bioinformatics* **35**:4453–4455. doi:10.1093/bioinformatics/btz305

Kozmik Z, Ruzickova J, Jonasova K, Matsumoto Y, Vopalensky P, Kozmikova I, Strnad H, Kawamura S, Piatigorsky J, Paces V, Vlcek C. 2008. Assembly of the cnidarian camera-type eye from vertebrate-like components. *Proc Natl Acad Sci U S A* **105**:8989–8993. doi:10.1073/pnas.0800388105

Levy S, Elek A, Grau-Bové X, Menéndez-Bravo S, Iglesias M, Tanay A, Mass T, Sebé-Pedrós A. 2021. A stony coral cell atlas illuminates the molecular and cellular basis of coral symbiosis, calcification, and immunity. *Cell* **184**:2973–2987. doi:10.1016/j.cell.2021.04.005

Maier JA, Martinez C, Kasavajhala K, Wickstrom L, Hauser KE, Simmerling C. 2015. Ff14SB: improving the accuracy of protein side chain and backbone parameters from ff99SB. *J Chem Theory Comput* **11**:3696–3713. doi:10.1021/acs.jctc.5b00255

Mason BM, Koyanagi M, Sugihara T, Iwasaki M, Slepak V, Miller DJ, Sakai Y, Terakita A. 2023. Multiple opsins in a reef-building coral, Acropora millepora. *Sci Rep* **13**:1628. doi:10.1038/s41598-023-28476-5

Mayol E, García-Recio A, Tiemann JKS, Hildebrand PW, Guixà-González R, Olivella M, Cordomí A. 2020. HomolWat: a web server tool to incorporate 'homologous' water molecules into GPCR structures. *Nucleic Acids Res* **48**:W54–W59. doi:10.1093/nar/gkaa440

Metz S, Kästner J, Sokol AA, Keal TW, Sherwood P. 2014. ChemShell—a modular software package for QM/MM simulations. *Wiley Interdiscip Rev Comput Mol Sci* **4**:101–110. doi:10.1002/wcms.1163

Mizuno M, Nakajima A, Kandori H, Mizutani Y. 2018. Structural evolution of a retinal chromophore in the photocycle of halorhodopsin from Natronobacterium pharaonis. *J Phys Chem A* **122**:2411–2423. doi:10.1021/acs.jpca.7b12332

Mous S, Gotthard G, Ehrenberg D, Sen S, Weinert T, Johnson PJM, James D, Nass K, Furrer A, Kekilli D, Ma P, Brünle S, Casadei CM, Martiel I, Dworkowski F, Gashi D, Skopintsev P, Wranik M, Knopp G, Panepucci E, Panneels V, Cirelli C, Ozerov D, Schertler GFX, Wang M, Milne C, Standfuss J, Schapiro I, Heberle J, Nogly P. 2022. Dynamics and mechanism of a light-driven chloride pump. *Science* **375**:845–851. doi:10.1126/science.abj6663

Mroginski M-A, Adam S, Amoyal GS, Barnoy A, Bondar A-N, Borin VA, Church JR, Domratcheva T, Ensing B, Fanelli F, Ferré N, Filiba O, Pedraza-González L, González R, González-Espinoza CE, Kar RK, Kemmler L, Kim SS, Kongsted J, Krylov AI, Lahav Y, Lazaratos M, NasserEddin Q, Navizet I, Nemukhin A, Olivucci M, Olsen JMH, Pérez de Alba Ortíz A, Pieri E, Rao AG, Rhee YM, Ricardi N, Sen S, Solov'yov IA, De Vico L, Wesolowski TA, Wiebeler C, Yang X, Schapiro I. 2021. Frontiers in multiscale modeling of photoreceptor proteins. *Photochem Photobiol* **97**:243–269. doi:10.1111/php.13372

Nagata T, Koyanagi M, Tsukamoto H, Mutt E, Schertler GFX, Deupi X, Terakita A. 2019. The counterion–retinylidene Schiff base interaction of an invertebrate rhodopsin rearranges upon light activation. *Commun Biol* **2**:180. doi:10.1038/s42003-019-0409-3

Nathans J. 1990. Determinants of visual pigment absorbance: identification of the retinylidene Schiff's base counterion in bovine rhodopsin. *Biochemistry* **29**:9746–9752. doi:10.1021/bi00493a034

Neese F. 2022. Software update: the ORCA program system—version 5.0. *Wiley Interdiscip Rev Comput Mol Sci* **12**. doi:10.1002/wcms.1606

Obayashi K, Zou R, Kawaguchi T, Mori T, Tsukamoto H. 2025. Molecular basis underlying the specificity of an antagonist AA92593 for mammalian melanopsins. *J Biol Chem* **301**:108461. doi:10.1016/j.jbc.2025.108461

Olsson MHM, Søndergaard CR, Rostkowski M, Jensen JH. 2011. PROPKA3: consistent treatment of internal and surface residues in empirical pKa predictions. *J Chem Theory Comput* **7**:525–537. doi:10.1021/ct100578z

Picciani N, Kerlin JR, Sierra NC, Swafford AJM, Ramirez MD, Cannon JT, Daly M, Oakley TH. 2018. Prolific origination of eyes in cnidaria with co-option of non-visual opsins. *Curr Biol* **28**:2413-2419.e4. doi:10.2139/ssrn.3155889

Pitt GA, Collins FD, Morton RA, Stok P. 1955. Studies on rhodopsin. VIII. Retinylidenemethylamine, an indicator yellow analogue. *Biochem J* **59**:122–128. doi:10.1042/bj0590122

Ramirez MD, Pairett AN, Pankey MS, Serb JM, Speiser DI, Swafford AJ, Oakley TH. 2016. The last common ancestor of most bilaterian animals possessed at least nine opsins. *Genome Biol Evol* **8**:3640–3652. doi:10.1093/gbe/evw248

Ridge KD, Abdulaev NG. 2000. Folding and assembly of rhodopsin from expressed fragments. *Methods Enzymol* **315**:59–70. doi:10.1016/s0076-6879(00)15834-3

Runge E, Gross EKU. 1984. Density-functional theory for time-dependent systems. *Phys Rev Lett* **52**:997–1000. doi:10.1103/physrevlett.52.997

Ryckaert J-P, Ciccotti G, Berendsen HJC. 1977. Numerical integration of the cartesian equations of motion of a system with constraints: molecular dynamics of n-alkanes. *J Comput Phys* **23**:327–341. doi:10.1016/0021-9991(77)90098-5

Sakai K, Ikeuchi H, Fujiyabu C, Imamoto Y, Yamashita T. 2022. Convergent evolutionary counterion displacement of bilaterian opsins in ciliary cells. *Cell Mol Life Sci* **79**:493. doi:10.1007/s00018-022-04525-6

Sakmar TP, Franke RR, Khorana HG. 1991. The role of the retinylidene Schiff base counterion in rhodopsin in determining wavelength absorbance and Schiff base pK_a. *Proc Natl Acad Sci U S A* **88**:3079–3083. doi:10.1073/pnas.88.8.3079

Sakmar TP, Franke RR, Khorana HG. 1989. Glutamic acid-113 serves as the retinylidene Schiff base counterion in bovine rhodopsin. *Proc Natl Acad Sci U S A* **86**:8309–8313. doi:10.1073/pnas.86.21.8309

Scharf B, Engelhard M. 1994. Blue halorhodopsin from Natronobacterium pharaonis: wavelength regulation by anions. *Biochemistry* **33**:6387–6393. doi:10.1021/bi00187a002

Senn HM, Thiel W. 2009. QM/MM methods for biomolecular systems. *Angew Chem Int Ed Engl* **48**:1198–1229. doi:10.1002/anie.200802019

Sherwood P, de Vries AH, Guest MF, Schreckenbach G, Catlow CRA, French SA, Sokol AA, Bromley ST, Thiel W, Turner AJ, Billeter S, Terstegen F, Thiel S, Kendrick J, Rogers SC, Casci J, Watson M, King F, Karlsen E, Sjøvoll M, Fahmi A, Schäfer A, Lennartz C. 2003. QUASI: a general purpose implementation of the QM/MM approach and its application to problems in catalysis. *J Mol Struct (THEOCHEM)* **632**:1–28. doi:10.1016/s0166-1280(03)00285-9

Shichida Y, Kato T, Sasayama S, Fukada Y, Yoshizawa T. 1990. Effects of chloride on chicken iodopsin and the chromophore transfer reactions from iodopsin to scotopsin and B-photopsin. *Biochemistry* **29**:5843–5848. doi:10.1021/bi00476a028

Shihoya W, Inoue K, Singh M, Konno M, Hososhima S, Yamashita K, Ikeda K, Higuchi A, Izume T, Okazaki S, Hashimoto M, Mizutori R, Tomida S, Yamauchi Y, Abe-Yoshizumi R, Katayama K, Tsunoda SP, Shibata M, Furutani Y, Pushkarev A, Béjà O, Uchihashi T, Kandori H, Nureki O. 2019. Crystal structure of heliorhodopsin. *Nature* **574**:132–136. doi:10.1038/s41586-019-1604-6

Shinzato C, Khalturin K, Inoue J, Zayasu Y, Kanda M, Kawamitsu M, Yoshioka Y, Yamashita H, Suzuki G, Satoh N. 2020. Eighteen coral genomes reveal the evolutionary origin of Acropora strategies to accommodate environmental changes. *Mol Biol Evol* **38**:16–30. doi:10.1093/molbev/msaa216

Sinha A, Jones Brunette AM, Fay JF, Schafer CT, Farrens DL. 2014. Rhodopsin TM6 can interact with two separate and distinct sites on arrestin: evidence for structural plasticity and multiple docking modes in arrestin-rhodopsin binding. *Biochemistry* **53**:3294–3307. doi:10.1021/bi401534y

Søndergaard CR, Olsson MHM, Rostkowski M, Jensen JH. 2011. Improved treatment of ligands and coupling effects in empirical calculation and rationalization of pKa values. *J Chem Theory Comput* **7**:2284–2295. doi:10.1021/ct200133y

Steinberg G, Ottolenghi M, Sheves M. 1993. pKa of the protonated Schiff base of bovine rhodopsin. A study with artificial pigments. *Biophys J* **64**:1499–1502. doi:10.1016/S0006-3495(93)81518-2

Suga H, Schmid V, Gehring WJ. 2008. Evolution and functional diversity of jellyfish opsins. *Curr Biol* **18**:51–55. doi:10.1016/j.cub.2007.11.059

Terakita A. 2005. The opsins. *Genome Biol* **6**:213. doi:10.1186/gb-2005-6-3-213

Terakita A, Hara R, Hara T. 1989. Retinal-binding protein as a shuttle for retinal in the rhodopsin-retinochrome system of the squid visual cells. *Vision Res* **29**:639–652. doi:10.1016/0042-6989(89)90026-6

Terakita A, Kawano-Yamashita E, Koyanagi M. 2012. Evolution and diversity of opsins. *Wiley Interdiscip Rev Membr Transp Signal* **1**:104–111. doi:10.1002/wmts.6

Terakita A, Koyanagi M, Tsukamoto H, Yamashita T, Miyata T, Shichida Y. 2004. Counterion displacement in the molecular evolution of the rhodopsin family. *Nat Struct Mol Biol* **11**:284–289. doi:10.1038/nsmb731

Terakita A, Yamashita T, Shichida Y. 2000. Highly conserved glutamic acid in the extracellular IV–V loop in rhodopsins acts as the counterion in retinochrome, a member of the rhodopsin family. *Proceedings of the National Academy of Sciences* **97**:14263–14267. doi:10.1073/pnas.260349597

Tsutsui K, Shichida Y. 2010. Photosensitivities of rhodopsin mutants with a displaced counterion. *Biochemistry* **49**:10089–10097. doi:10.1021/bi101020p

Venn AA, Tambutté E, Lotto S, Zoccola D, Allemand D, Tambutté S. 2009. Imaging intracellular pH in a reef coral and symbiotic anemone. *Proc Natl Acad Sci U S A* **106**:16574–16579. doi:10.1073/pnas.0902894106

Voolstra CR, Miller DJ, Ragan MA, Hoffmann AA, Hoegh-Guldberg O, Bourne DG, Ball EE, Ying H, Forêt S, Takahashi S, Weynberg KD, van Oppen MJH, Morrow K, Chan CX, Rosic N, Leggat W, Sprungala S, Imelfort M, Tyson GW, Kassahn KS, Lundgren PB, Beeden RJ, Ravasi T, Berumen ML, Abal E, Fyffe T. 2015. The ReFuGe 2020 Consortium—using “omics” approaches to explore the adaptability and resilience of coral holobionts to environmental change. *Front Mar Sci* **2**:68. doi:10.3389/fmars.2015.00068

Weigend F. 2008. Hartree-Fock exchange fitting basis sets for H to Rn. *J Comput Chem* **29**:167–175. doi:10.1002/jcc.20702

Yanai T, Tew DP, Handy NC. 2004. A new hybrid exchange–correlation functional using the Coulomb-attenuating method (CAM-B3LYP). *Chem Phys Lett* **393**:51–57. doi:10.1016/j.cplett.2004.06.011

Zhukovsky EA, Oprian DD. 1989. Effect of carboxylic acid side chains on the absorption maximum of visual pigments. *Science* **246**:928–930. doi:10.1126/science.2573154

Figures

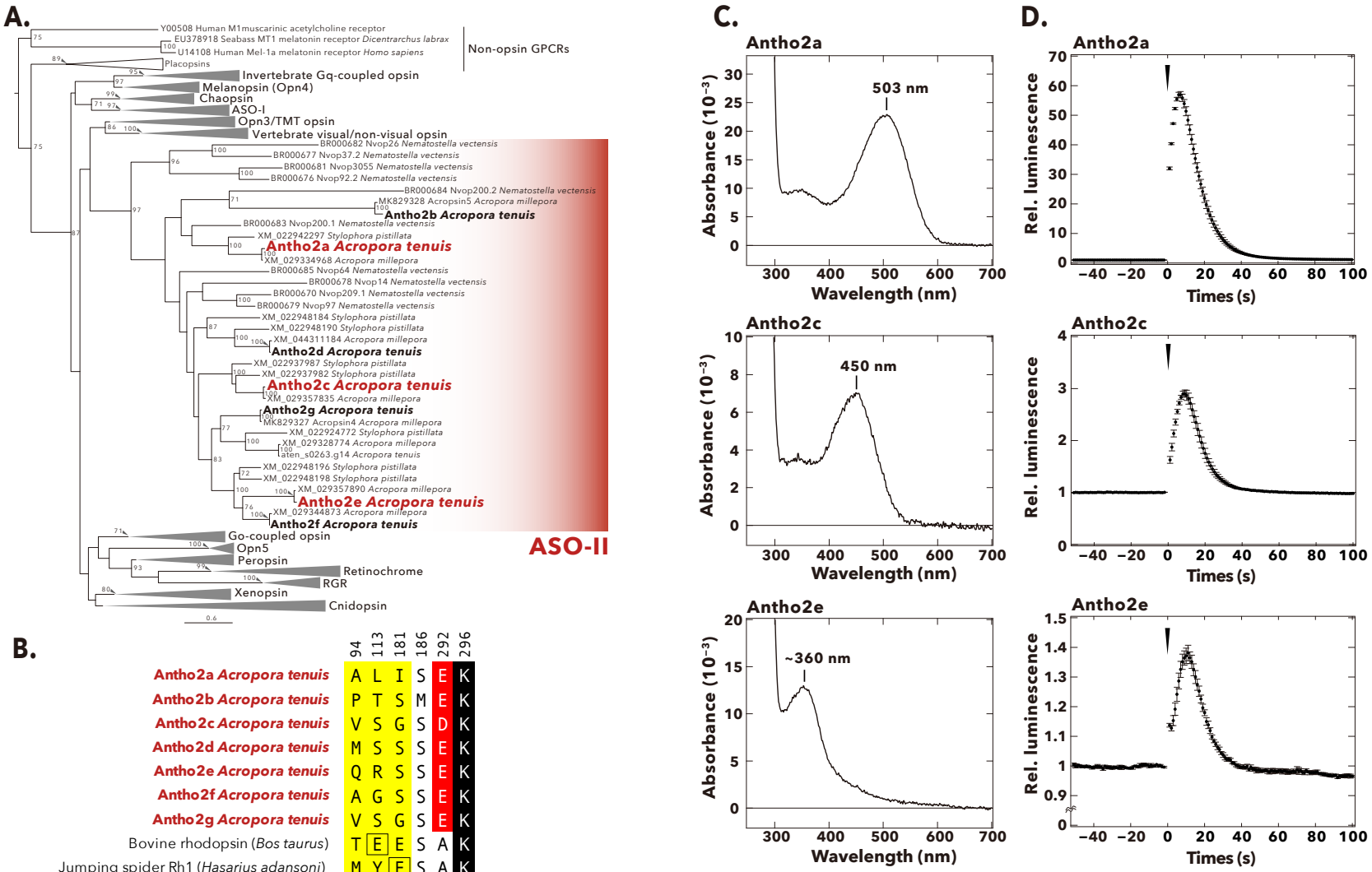
A.
Y00508 Human M1muscarinic acetylcholine receptor
EU378918 Seabass MT1 melatonin receptor Dicentrarchus labrax
U14108 Human Mel-1a melatonin receptor Homo sapiens
Non-opsin GPCRs
Placopsins
Invertebrate Gq-coupled opsin
Melanopsin (Opn4)
Chaopsin
ASO-I
Opn3/TMT opsin
Vertebrate visual/non-visual opsin
BR000682 Nvop26 Nematostella vectensis
BR000677 Nvop37.2 Nematostella vectensis
BR000681 Nvop3055 Nematostella vectensis
BR000676 Nvop92.2 Nematostella vectensis
BR000684 Nvop200.2 Nematostella vectensis
MK829328 Acropsin5 Acropora millepora
Antho2b Acropora tenuis
BR000683 Nvop200.1 Nematostella vectensis
XM_022942297 Stylophora pistillata
Antho2a Acropora tenuis
XM_029334968 Acropora millepora
BR000685 Nvop64 Nematostella vectensis
BR000678 Nvop14 Nematostella vectensis
BR000670 Nvop209.1 Nematostella vectensis
BR000679 Nvop97 Nematostella vectensis
XM_022948184 Stylophora pistillata
XM_022948190 Stylophora pistillata
XM_044311184 Acropora millepora
Antho2d Acropora tenuis
XM_022937987 Stylophora pistillata
XM_022937982 Stylophora pistillata
Antho2c Acropora tenuis
XM_029357835 Acropora millepora
Antho2g Acropora tenuis
MK829327 Acropsin4 Acropora millepora
XM_022924772 Stylophora pistillata
XM_029328774 Acropora millepora
aten_s0263.g14 Acropora tenuis
XM_022948196 Stylophora pistillata
XM_022948198 Stylophora pistillata
XM_029357890 Acropora millepora
Antho2e Acropora tenuis
XM_029344873 Acropora millepora
Antho2f Acropora tenuis
ASO-II
Go-coupled opsin
Opn5
Peropsin
Retinochrome
RGR
Xenopsin
Cnidopsin
0.6
B.
94 113 181 186 292 296
Antho2a Acropora tenuis A L I S E K
Antho2b Acropora tenuis P T S M E K
Antho2c Acropora tenuis V S G S D K
Antho2d Acropora tenuis M S S S E K
Antho2e Acropora tenuis Q R S S E K
Antho2f Acropora tenuis A G S S E K
Antho2g Acropora tenuis V S G S E K
Bovine rhodopsin (Bos taurus) T E E S A K
Jumping spider Rh1 (Hasarius adansoni) M Y E S A K
Jellyfish Opsin (Carybrea rastoni) E A E R A K
C.
Antho2a
503 nm
Absorbance (10⁻³)
Wavelength (nm)
Antho2c
450 nm
Antho2e
~360 nm
D.
Antho2a
Antho2c
Antho2e
Rel. luminescence
Times (s)

825 **Fig. 1. Phylogenetic tree, selected amino acid residues, absorption spectra, and light-induced**
826 **Ca^{2+} responses of *Acropora tenuis* opsins belonging to the ASO-II group. (A)** Maximum-likelihood
827 (ML) tree of animal opsins including *A. tenuis* opsins in the ASO-II group. Seven opsins in the ASO-II
828 group that were identified and cloned from *A. tenuis* in this study are shown in bold and the three
829 members for which we obtained absorption spectra are highlighted in red. Numbers at the nodes
830 represent support values of each ML branch estimated by 1000 bootstrap samplings (≥ 70% are
831 indicated). Scale bar = 0.6 substitutions per site. All branches and support values are provided in Fig.
832 S1. **(B)** Selected residues near the Schiff base in opsins of the ASO-II group and other animal opsins.
833 Animal opsins typically have an acidic residue acting as counterion at one of three established sites
834 (yellow): E94 (e.g., jellyfish opsin), E113 (e.g., bovine rhodopsin), or E181 (e.g., jumping spider
835 Rh1). Remarkably, opsins in the ASO-II group lack an acidic residue at any of these positions, but
836 instead feature an acidic residue at position 292 (red). The retinal-binding lysine, Lys296, is shown in
837 black. A more detailed sequence alignment is provided in Fig. S2. Residues are numbered according to
838 bovine rhodopsin. **(C)** Absorption spectra in the dark of three *A. tenuis* opsins in the ASO-II group
839 (Antho2a, Antho2c and Antho2e). The absorption spectra were measured at 0°C in 140 mM NaCl at
840 pH 6.5. The number in each graph shows the λ_{max} value. **(D)** Results of the aequorin-based
841 bioluminescent reporter assay for monitoring light-induced changes in Ca^{2+} in HEK293S cells
842 expressing the same three opsins in the ASO-II group as in panel C. In each graph, luminescence
843 values were normalized to the baseline. Black circles with error bars indicate the means ± SEMs (n =
844 3) of the measured relative luminescence. Black arrowheads at time 0 indicate the timing of one-
845 minute irradiation with green (495 nm; for Antho2a and Antho2c) or UV (395 nm; for Antho2e) light.

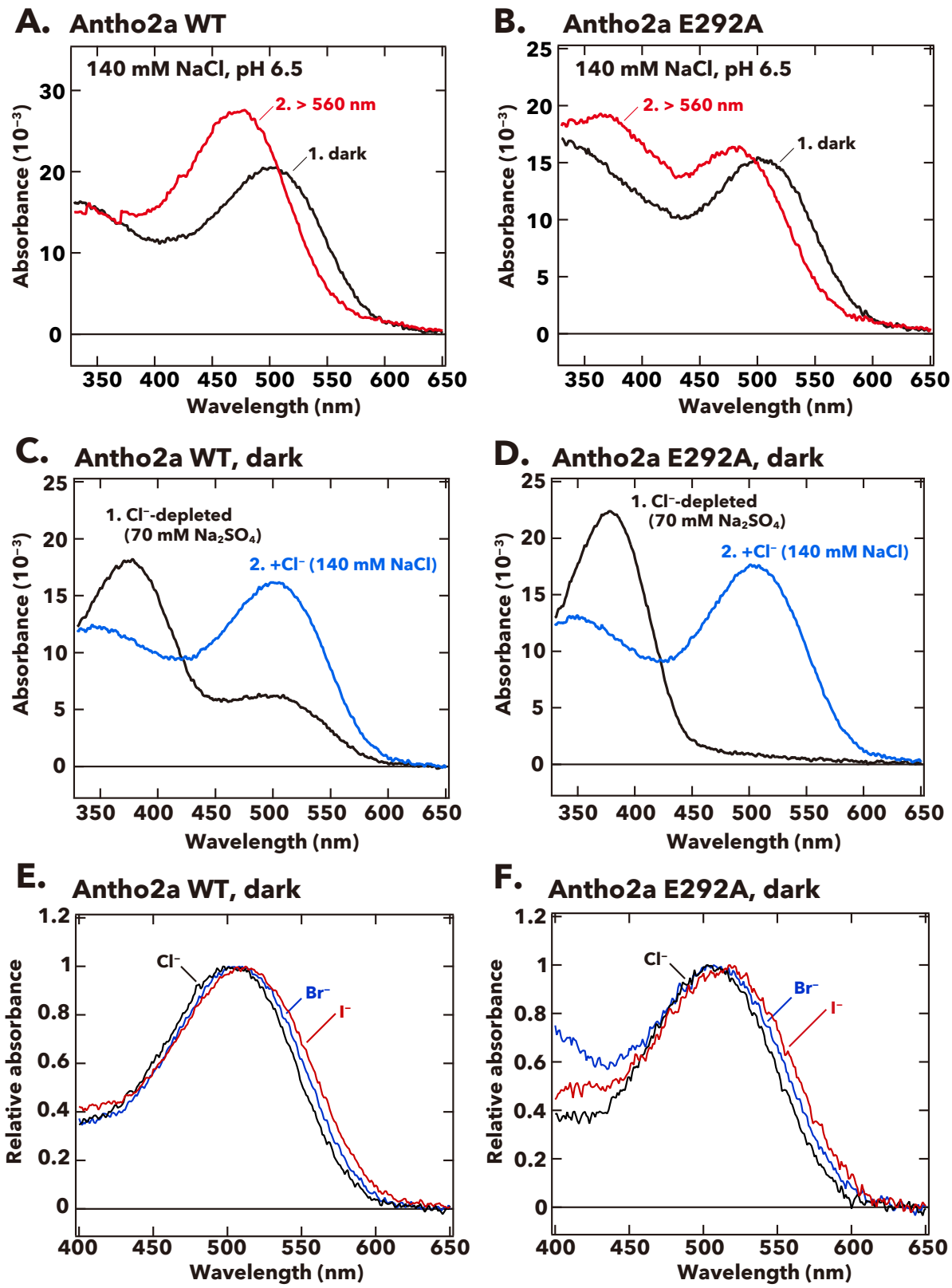
A. Antho2a WT
140 mM NaCl, pH 6.5
2. > 560 nm
1. dark
Absorbance (10⁻³)
Wavelength (nm)
B. Antho2a E292A
140 mM NaCl, pH 6.5
2. > 560 nm
1. dark
Absorbance (10⁻³)
Wavelength (nm)
C. Antho2a WT, dark
1. Cl⁻-depleted (70 mM Na₂SO₄)
2. +Cl⁻ (140 mM NaCl)
Absorbance (10⁻³)
Wavelength (nm)
D. Antho2a E292A, dark
1. Cl⁻-depleted (70 mM Na₂SO₄)
2. +Cl⁻ (140 mM NaCl)
Absorbance (10⁻³)
Wavelength (nm)
E. Antho2a WT, dark
Cl⁻
Br⁻
I⁻
Relative absorbance
Wavelength (nm)
F. Antho2a E292A, dark
Cl⁻
Br⁻
I⁻
Relative absorbance
Wavelength (nm)

Fig. 2

847 **Fig. 2. Absorption spectra of wild type and the E292A mutant of *A. tenuis* Antho2a. (A, B)**
848 Absorption spectra of the dark state (curve 1, black) and the photoproduct (curve 2, red) of the wild
849 type (Antho2a WT, **A**) and the E292A mutant (Antho2a E292A, **B**) at 140 mM NaCl and pH 6.5. The
850 samples were kept at 0°C during the spectroscopic measurements**. (C, D)** Absorption spectra of the
851 dark state of Antho2a WT **(C)** and Antho2a E292A **(D)** prepared in Cl^--depleted conditions, before
852 (curve 1, black) and after (curve 2, blue) adding Cl^- (see Materials and Methods for details). In the
853 Cl^--depleted condition, the pigments were solubilized in 70 mM Na_2SO_4, which reportedly does not
854 access to the Cl^- binding site in the chicken red-sensitive cone visual pigment iodosin (Shichida et al.,
855 1990), to moderate protein denaturation. **(E, F)** Effect of halide anions on the absorption spectra of
856 wild type Antho2a **(E)** and the Antho2a E292A mutant **(F)** at pH 6.5 and 0°C. The graphic shows the
857 normalized absorption spectra of the pigments prepared in 140 mM NaCl (black curves), 140 mM
858 NaBr (blue curves), and 140 mM NaI (red curves).

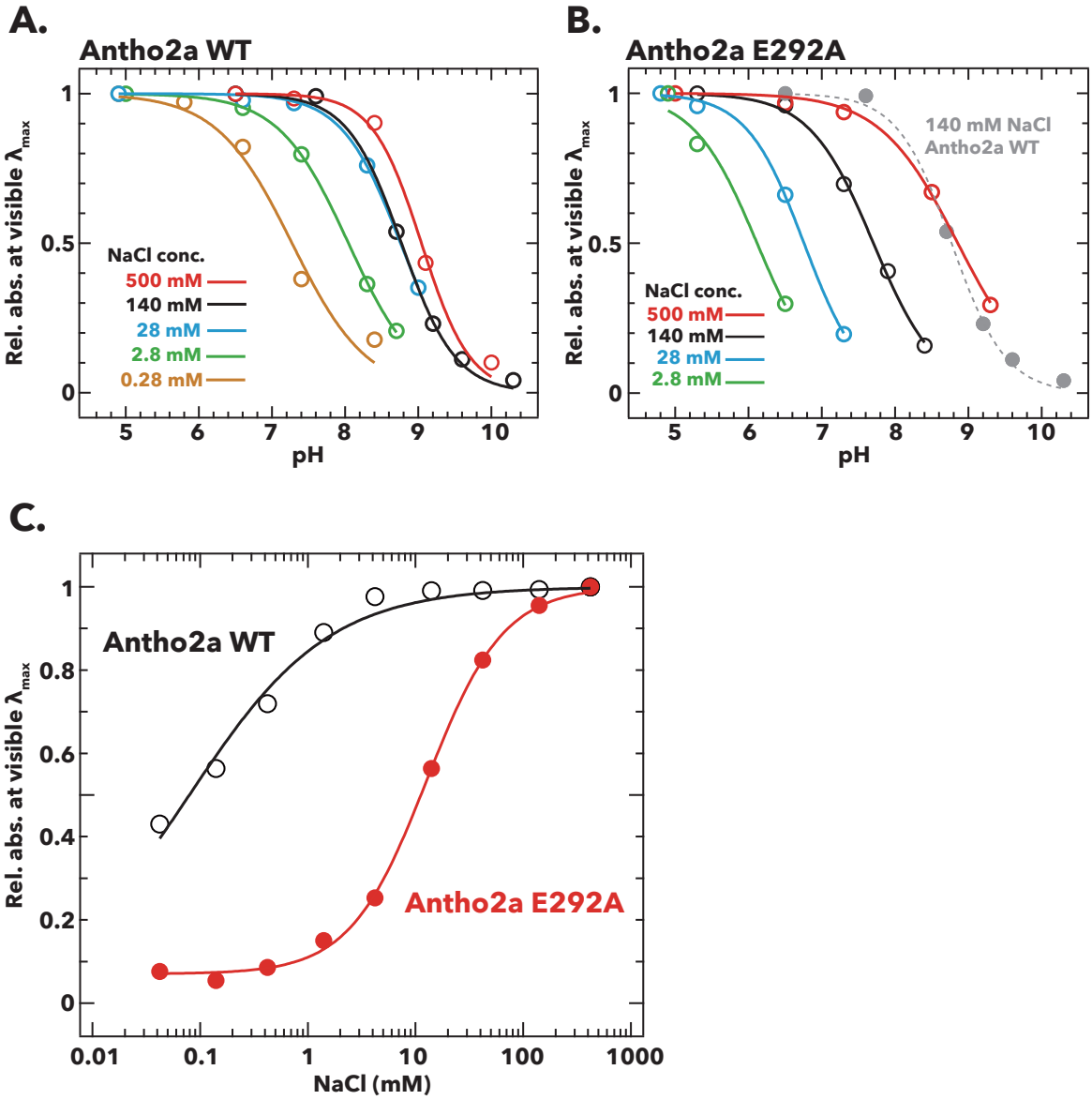

Fig. 3

Fig. 3. Effects of pH and Cl^- concentration on the absorption spectra of the dark states of wild type Antho2a and the Antho2a E292A mutant. (A, B) Changes in the absorbance at λ_{max} as a function of pH for **(A)** wild type Antho2a and **(B)** the E292A mutant at different Cl^- concentrations. The absorbance values at "visible λ_{max}" (mean absorbance at 503 ± 5 nm for the wild type and 505 ± 5 nm for the E292A mutant, respectively) were normalized for each Cl^- concentration to those at the lowest pH, in which the Schiff base is assumed to be fully protonated ("Rel. abs. at visible λ_{max}" in the y-axes). Solid and dashed lines represent sigmoid fits to the experimental data for each Cl^-

concentration (indicated by different colors). The pH-dependent change of wild type Antho2a at 140mM NaCl is also shown in panel B (dotted grey line). The full absorption spectra used to generate these plots are provided in Fig. S6 (for wild type Antho2a) and Fig. S8 (for the E292A mutant). **(C)** Changes in the absorbance at λ_{max} for wild type Antho2a (black open circles) and the E292A mutant (red solid circles) as a function of Cl^- concentration. The absorbance values at visible λ_{max} were normalized to those at 500 mM NaCl for both the wild type and the E292A mutant. The lines in the graph were generated by fitting the Hill equation to the experimental data. The full absorption spectra used to generate these plots are provided in Fig. S9.

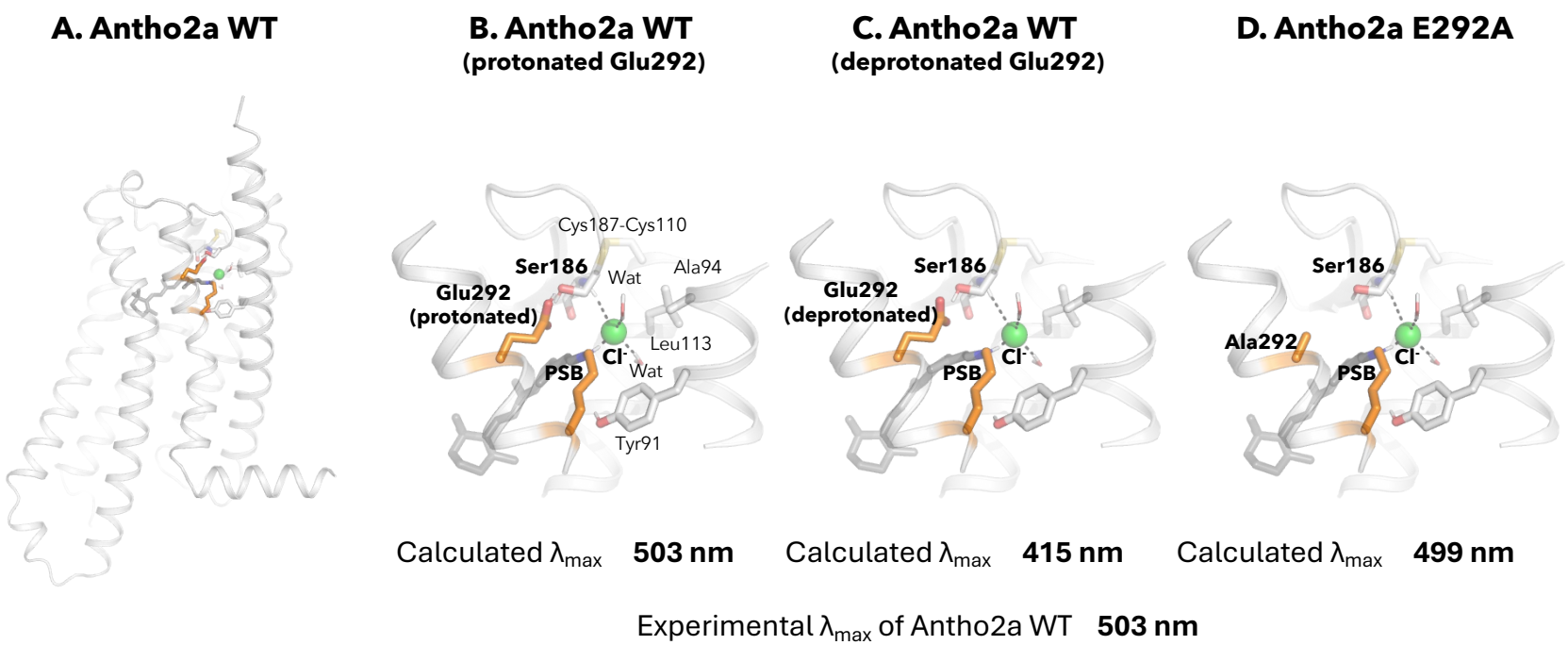

Fig. 4. QM/MM structural model of wild type Antho2a in the dark state (A) and detailed views of the retinal binding pocket with a protonated (neutral) Glu292 (B), a deprotonated (negatively charged) Glu292 (C), and the E292A mutant (D). The retinal protonated Schiff base (PSB) and the binding pocket residues are shown as sticks (including polar hydrogens) and the Cl^- ion as a sphere with its coordination shown as dashes. "Wat" indicates a water molecule. Residues in the QM region are marked in bold.

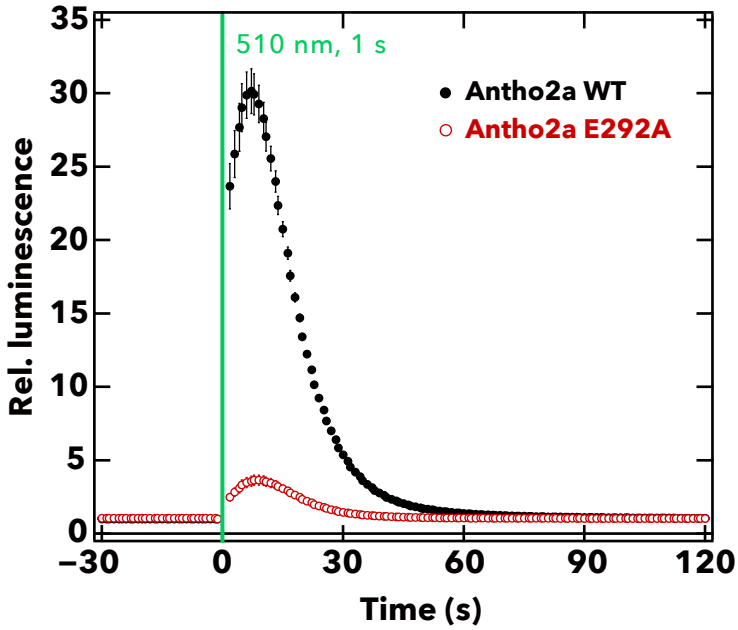

Fig. 5. Comparison of the light-evoked intracellular Ca^{2+} levels between wild type Antho2a and the E292A mutant. The graph shows the mean ± S.E.M (n = 4) of the measured relative luminescence values (luminescence values normalized to the baseline) for wild type Antho2a (black) and the E292A mutant (red) at pH7.0. The green vertical line indicates the time of cell illumination with green light (510 nm, for 1 s, 1.65×10^{15} photons/cm^2/s).

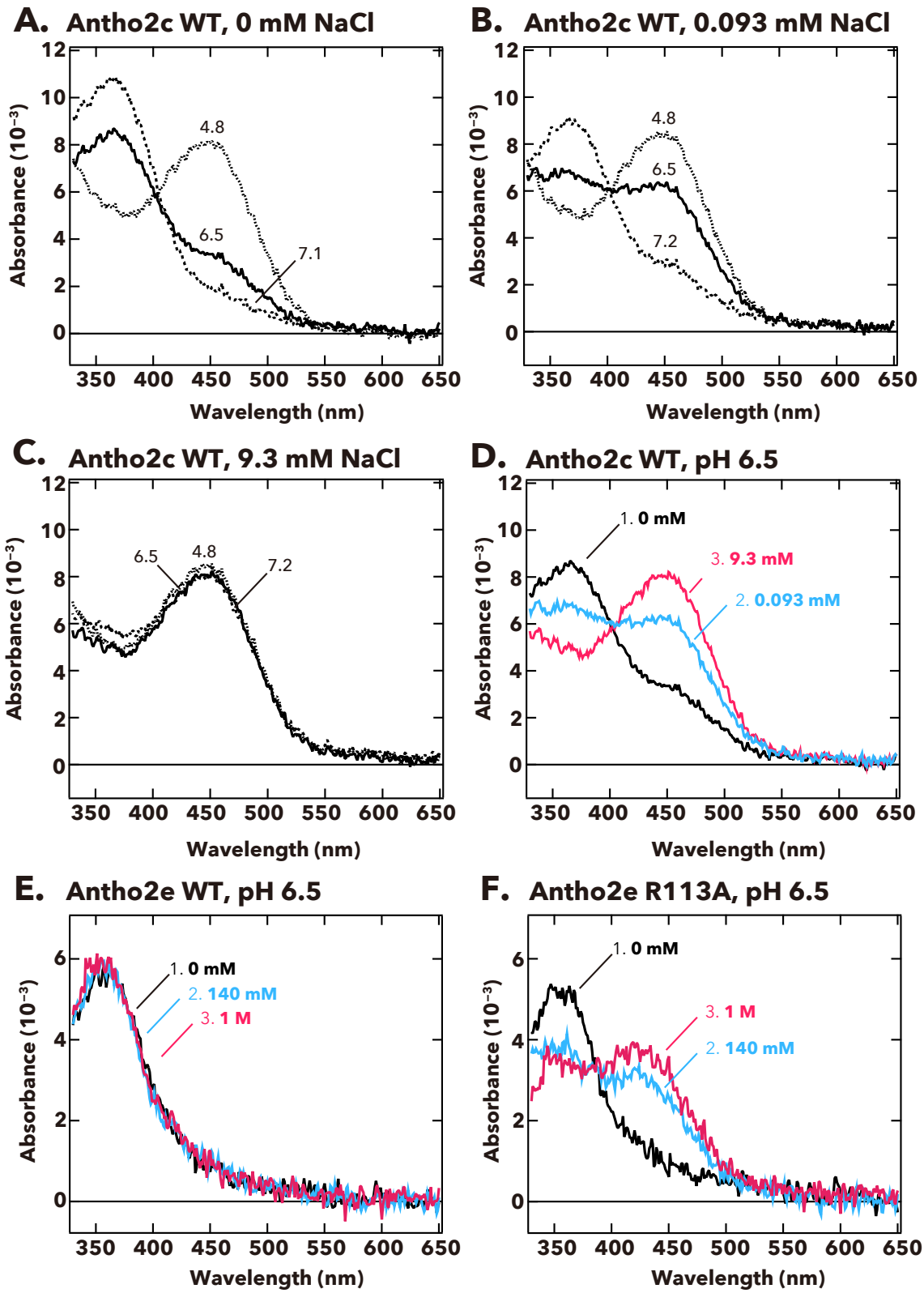
A. Antho2c WT, 0 mM NaCl
B. Antho2c WT, 0.093 mM NaCl
C. Antho2c WT, 9.3 mM NaCl
D. Antho2c WT, pH 6.5
E. Antho2e WT, pH 6.5
F. Antho2e R113A, pH 6.5
Absorbance (10⁻³)
Wavelength (nm)
4.8
6.5
7.1
7.2
1. 0 mM
2. 0.093 mM
3. 9.3 mM
2. 140 mM
3. 1 M

Fig. 6

886

887 **Fig. 6. pH-dependent changes in the absorption spectra of Antho2c and Antho2e at different Cl^-**

888 **concentrations at 0°C. (A–C)** Absorption spectra of purified wild type Antho2c pigment at **(A)** 0

889 mM, **(B)** 0.093 mM, and **(C)** 9.3 mM NaCl concentrations. The corresponding pH values are indicated

890 on each curve in the graphs. **(D)** Summary of the spectral changes for wild type Antho2c across

891 different Cl^- concentrations at neutral pH (pH 6.5). **(E, F)** Absorption spectra of **(E)** wild type Antho2e

892 (Antho2e WT) and **(F)** its R113A mutant (Antho2e R113A) at different Cl^- concentrations at pH 6.5 at

893 0°C. Each color indicates a different Cl^- concentration.

Supplementary table and figures

Table S1. Vertical excitation energies (ΔE_{calc}) and oscillator strengths (f) computed by quantum mechanics/molecular mechanics (QM/MM) calculations using different QM methods with the cc-pVTZ basis set.

QM Region	**sTD-DFT CAM-B3LYP**		**ADC(2)**	
	ΔE_{calc} nm (eV)	**f**	**ΔE_{calc} nm (eV)**	**f**
RET+Lyr296+Cl+Ser186+**Glu292 (deprotonated)**	415 (2.99)	1.54	374 (3.32)	1.64
RET+Lyr296+Cl+Ser186+**Glu292 (protonated)**	503 (2.47)	1.19	416 (2.98)	1.43
RET+Lyr296+Cl+Ser186+**Ala292**	499 (2.49)	1.19	426 (2.91)	1.36

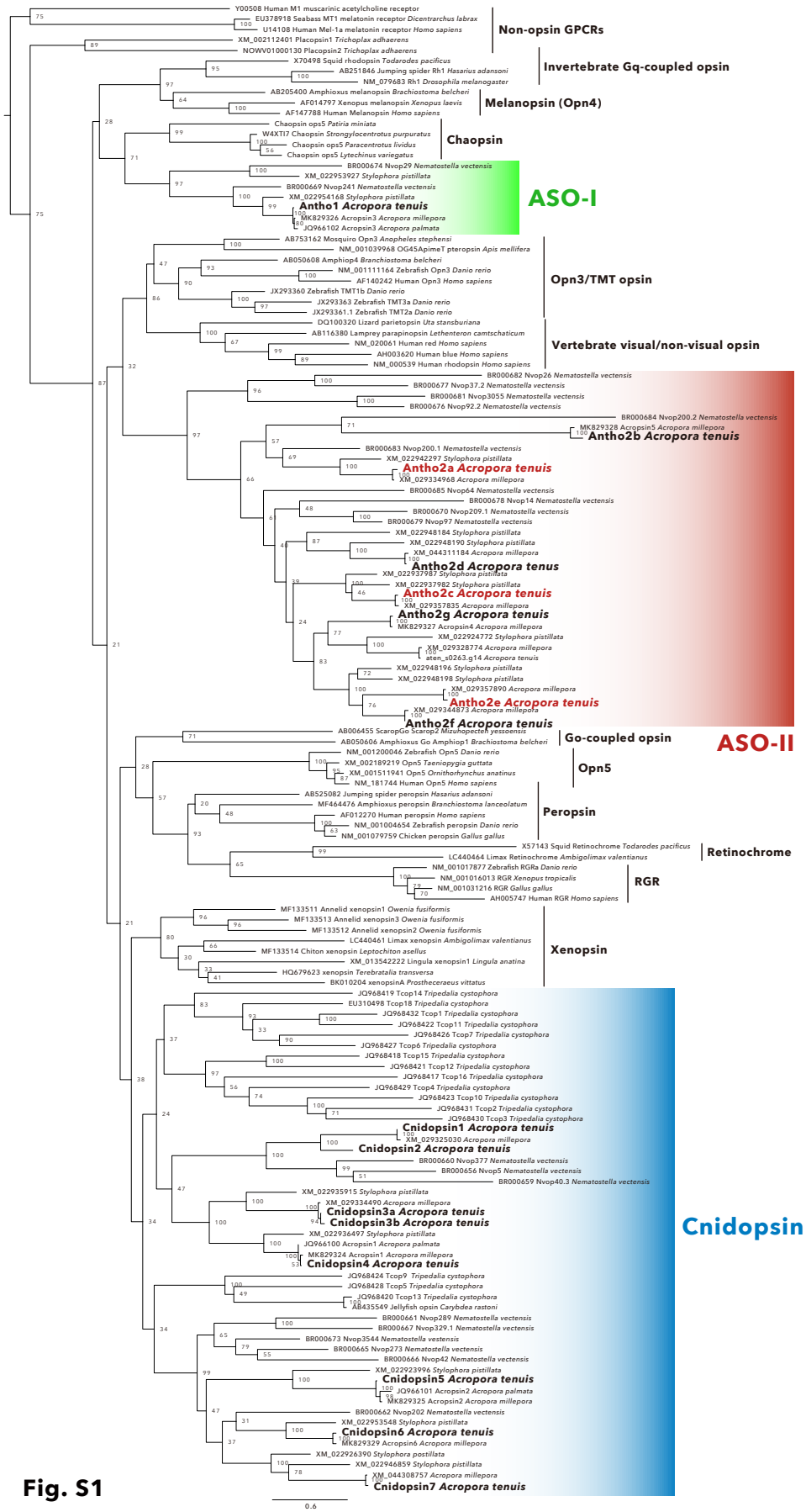
Y00508 Human M1 muscarinic acetylcholine receptor
EU378918 Seabass MT1 melatonin receptor Dicentrarchus labrax
U14108 Human Mel-1a melatonin receptor Homo sapiens
Non-opsin GPCRs
XM_002112401 Placopsin1 Trichoplax adhaerens
NOWV01000130 Placopsin2 Trichoplax adhaerens
X70498 Squid rhodopsin Todarodes pacificus
AB251846 Jumping spider Rh1 Hasarius adansoni
NM_079683 Rh1 Drosophila melanogaster
Invertebrate Gq-coupled opsin
AB205400 Amphioxus melanopsin Brachiostoma belcheri
AF014797 Xenopus melanopsin Xenopus laevis
AF147788 Human Melanopsin Homo sapiens
Melanopsin (Opn4)
Chaopsin ops5 Patiria miniata
W4XTI7 Chaopsin Strongylocentrotus purpuratus
Chaopsin ops5 Paracentrotus lividus
Chaopsin ops5 Lytechinus variegatus
Chaopsin
BR000674 Nvop29 Nematostella vectensis
XM_022953927 Stylophora pistillata
BR000669 Nvop241 Nematostella vectensis
XM_022954148 Stylophora pistillata
Antho1 Acropora tenuis
MK829326 Acropsin3 Acropora millepora
JQ966102 Acropsin3 Acropora palmata
ASO-I
AB753162 Mosquiro Opn3 Anopheles stephensi
NM_001039968 OG45ApimeT pteropsin Apis mellifera
AB050608 Amphiop4 Branchiostoma belcheri
NM_001111164 Zebrafish Opn3 Danio rerio
AF140242 Human Opn3 Homo sapiens
JX293360 Zebrafish TMT1b Danio rerio
JX293363 Zebrafish TMT3a Danio rerio
JX293361.1 Zebrafish TMT2a Danio rerio
Opn3/TMT opsin
DQ100320 Lizard parietopsin Uta stansburiana
AB116380 Lamprey parapinopsin Lethenteron camtschaticum
NM_020061 Human red Homo sapiens
AH003620 Human blue Homo sapiens
NM_000539 Human rhodopsin Homo sapiens
Vertebrate visual/non-visual opsin
BR000682 Nvop26 Nematostella vectensis
BR000677 Nvop37.2 Nematostella vectensis
BR000681 Nvop3055 Nematostella vectensis
BR000676 Nvop92.2 Nematostella vectensis
BR000684 Nvop200.2 Nematostella vectensis
MK829328 Acropsin5 Acropora millepora
Antho2b Acropora tenuis
BR000683 Nvop200.1 Nematostella vectensis
XM_022942297 Stylophora pistillata
Antho2a Acropora tenuis
XM_029334968 Acropora millepora
BR000685 Nvop64 Nematostella vectensis
BR000678 Nvop14 Nematostella vectensis
BR000670 Nvop209.1 Nematostella vectensis
BR000679 Nvop97 Nematostella vectensis
XM_022948184 Stylophora pistillata
XM_022948190 Stylophora pistillata
XM_044311184 Acropora millepora
Antho2d Acropora tenus
XM_022937987 Stylophora pistillata
XM_022937982 Stylophora pistillata
Antho2c Acropora tenuis
XM_029357835 Acropora millepora
Antho2g Acropora tenuis
MK829327 Acropsin4 Acropora millepora
XM_022924772 Stylophora pistillata
XM_029328774 Acropora millepora
aten_s0263.g14 Acropora tenuis
XM_022948196 Stylophora pistillata
XM_022948198 Stylophora pistillata
XM_029357890 Acropora millepora
Antho2e Acropora tenuis
XM_029344873 Acropora millepora
Antho2f Acropora tenuis
ASO-II
AB006455 ScaropGo Scarop2 Mizuhopecten yessoensis
AB050606 Amphioxus Go Amphiop1 Brachiostoma belcheri
Go-coupled opsin
NM_001200046 Zebrafish Opn5 Danio rerio
XM_002189219 Opn5 Taeniopygia guttata
XM_001511941 Opn5 Ornithorhynchus anatinus
NM_181744 Human Opn5 Homo sapiens
Opn5
AB525082 Jumping spider peropsin Hasarius adansoni
MF464476 Amphioxus peropsin Branchiostoma lanceolatum
AF012270 Human peropsin Homo sapiens
NM_001004654 Zebrafish peropsin Danio rerio
NM_001079759 Chicken peropsin Gallus gallus
Peropsin
X57143 Squid Retinochrome Todarodes pacificus
LC440464 Limax Retinochrome Ambigolimax valentianus
Retinochrome
NM_001017877 Zebrafish RGRa Danio rerio
NM_001016013 RGR Xenopus tropicalis
NM_001031216 RGR Gallus gallus
AH005747 Human RGR Homo sapiens
RGR
MF133511 Annelid xenopsin1 Owenia fusiformis
MF133513 Annelid xenopsin3 Owenia fusiformis
MF133512 Annelid xenopsin2 Owenia fusiformis
LC440461 Limax xenopsin Ambigolimax valentianus
MF133514 Chiton xenopsin Leptochiton asellus
XM_013542222 Lingula xenopsin1 Lingula anatina
HQ679623 xenopsin Terebratalia transversa
BK010204 xenopsinA Prostheceraeus vittatus
Xenopsin
JQ968419 Tcop14 Tripedalia cystophora
EU310498 Tcop18 Tripedalia cystophora
JQ968432 Tcop1 Tripedalia cystophora
JQ968422 Tcop11 Tripedalia cystophora
JQ968426 Tcop7 Tripedalia cystophora
JQ968427 Tcop6 Tripedalia cystophora
JQ968418 Tcop15 Tripedalia cystophora
JQ968421 Tcop12 Tripedalia cystophora
JQ968417 Tcop16 Tripedalia cystophora
JQ968429 Tcop4 Tripedalia cystophora
JQ968423 Tcop10 Tripedalia cystophora
JQ968431 Tcop2 Tripedalia cystophora
JQ968430 Tcop3 Tripedalia cystophora
Cnidopsin1 Acropora tenuis
XM_029325030 Acropora millepora
Cnidopsin2 Acropora tenuis
BR000660 Nvop377 Nematostella vectensis
BR000656 Nvop5 Nematostella vectensis
BR000659 Nvop40.3 Nematostella vectensis
XM_022935915 Stylophora pistillata
XM_029334490 Acropora millepora
Cnidopsin3a Acropora tenuis
Cnidopsin3b Acropora tenuis
XM_022936497 Stylophora pistillata
JQ966100 Acropsin1 Acropora palmata
MK829324 Acropsin1 Acropora millepora
Cnidopsin4 Acropora tenuis
JQ968424 Tcop9 Tripedalia cystophora
JQ968428 Tcop5 Tripedalia cystophora
JQ968420 Tcop13 Tripedalia cystophora
AB435549 Jellyfish opsin Carybdea rastoni
BR000661 Nvop289 Nematostella vectensis
BR000667 Nvop329.1 Nematostella vectensis
BR000673 Nvop3544 Nematostella vestensis
BR000665 Nvop273 Nematostella vectensis
BR000666 Nvop42 Nematostella vectensis
XM_022923996 Stylophora pistillata
Cnidopsin5 Acropora tenuis
JQ966101 Acropsin2 Acropora palmata
MK829325 Acropsin2 Acropora millepora
BR000662 Nvop202 Nematostella vectensis
XM_022953548 Stylophora pistillata
Cnidopsin6 Acropora tenuis
MK829329 Acropsin6 Acropora millepora
XM_022926390 Stylophora pastillata
XM_022946859 Stylophora pistillata
XM_044308757 Acropora millepora
Cnidopsin7 Acropora tenuis
Cnidopsin
0.6

Fig. S1

901 **Fig. S1. Maximum-likelihood (ML) tree of animal opsins, with non-opsin GPCRs included as an**
902 **outgroup** (a simplified version of the ML tree is shown in Fig. 1A). The tree includes opsins
903 belonging to the eight main groups (see main text) as well as of opsins from the recently identified
904 subgroups xenopsins and chaopsins (Ramirez MD et al. *Genome Biol Evol* **8**:3640–3652, 2016). The
905 sixteen *A. tenuis* opsins (eight opsins in the cnidopsin group, one opsin in the ASO-I group, and seven
906 opsins in the ASO-II group) that were identified in this study are shown in bold. The three opsins in
907 the ASO-II group for which absorption spectra were successfully obtained are highlighted in red.
908 Numbers at nodes represent support values for the ML branch estimated by 1000 bootstrap samplings
909 (≥ 70% are indicated). Scale bar = 0.6 substitutions per site.

	TM1	TM2		TM3		E(D)RY motif			ECL2			TM7		NPxxY motif				
Antho2a *Acropora tenuis*	Y	Y	A	L	N	M	S	Y	I	S	C	E	K	N	P	I	L	Y
Antho2b *Acropora tenuis*	L	Y	P	T	G	V	S	K	S	M	C	E	K	P	P	F	A	Y
Antho2c *Acropora tenuis*	Y	Y	V	S	N	V	M	F	G	S	C	D	K	N	P	I	V	Y
Antho2d *Acropora tenuis*	Y	Y	M	S	N	V	M	Y	S	S	C	E	K	N	P	I	V	Y
Antho2e *Acropora tenuis*	Y	Y	Q	R	N	V	S	Y	S	S	C	E	K	N	P	L	I	Y
Antho2f *Acropora tenuis*	Y	Y	A	G	N	V	S	Y	S	S	C	E	K	G	P	I	I	Y
Antho2g *Acropora tenuis*	Y	Y	V	S	N	V	I	N	G	S	C	E	K	N	P	V	V	Y
AB251846 Jumping spider Rh1 *Hasarius adansoni*	L	M	M	Y	G	D	R	Y	E	S	C	A	K	N	P	I	V	Y
Antho1 *Acropora tenuis*	S	N	S	Y	H	D	R	F	E	G	C	V	K	N	V	L	I	Y
AF140242 Human OPN3 *Homo sapiens*	L	V	T	D	G	E	R	Y	D	G	C	Y	K	N	P	V	I	Y
NP_001014890 Bovine rhodopsin *Bos taurus*	L	F	T	E	A	E	R	Y	E	S	C	A	K	N	P	V	I	Y
AB050606 Amphioxus amphiop1 *Brachiostoma belcheri*	S	Y	S	Y	C	Y	R	Y	E	T	C	S	K	N	P	I	I	Y
NM_181744 Human OPN5 *Homo sapiens*	A	K	T	Y	G	D	R	Y	E	S	C	T	K	N	P	I	I	Y
AF012270 Human peropsin *Homo sapiens*	V	Y	S	Y	N	D	R	Y	D	T	C	P	K	N	P	C	I	Y
X57143 Squid retinochrome *Todarodes pacificus*	T	D	H	M	G	E	R	Y	E	S	C	P	K	F	P	L	L	I
AH005747 Human RGR *Homo sapiens*	V	L	A	H	G	G	R	Y	E	C	C	A	K	N	A	I	N	Y
MF133514 Chiton xenopsin *Leptochiton asellus*	I	N	A	E	V	D	R	Y	E	S	C	A	K	N	P	I	I	Y
AB435549 Jellyfish opsin *Carybdea rastoni*	L	Y	E	A	I	D	R	Y	E	R	C	A	K	N	P	I	I	Y
Cnidopsin1 *Acropora tenuis*	F	V	S	H	I	G	K	Y	G	I	C	G	K	N	P	I	L	Y
Cnidopsin2 *Acropora tenuis*	F	V	S	H	V	G	K	Y	E	T	C	S	K	N	P	F	L	Y
Cnidopsin3a *Acropora tenuis*	F	L	L	Y	T	E	R	Y	E	S	C	A	K	N	P	F	I	Y
Cnidopsin3b *Acropora tenuis*	F	L	L	Y	T	E	R	Y	E	S	C	A	K	N	P	F	I	Y
Cnidopsin4 *Acropora tenuis*	F	L	L	T	A	E	R	Y	E	S	C	A	K	N	P	V	I	Y
Cnidopsin5 *Acropora tenuis*	S	M	G	Y	H	E	R	C	E	I	C	S	K	N	P	I	I	C
Cnidopsin6 *Acropora tenuis*	I	N	G	F	A	D	R	Y	E	A	C	S	K	N	P	I	I	Y
Cnidopsin7 *Acropora tenuis*	V	Y	A	Y	T	E	R	A	H	L	C	A	K	N	P	V	I	Y
	40	91	94	113	117	134	135	136	181	186	187	292	296	302	303			306

Fig. S2. Key residues in opsins of the ASO-II group and other animal opsins. Residues near the Schiff base were selected with reference to the crystal structure of bovine rhodopsin (PDB ID: 1U19) and the homology model of Antho2a (shown in Fig. 4). Position 292 contains an acidic residue (D/E) only in opsins of the ASO-II group (red). In addition, functionally important residues (such as the retinal binding Lys296 (black), the three established counterion sites (yellow), and two highly conserved motifs in Class A GPCRs, E(D)RY on TM3 (green) and NPxxY on TM7 (blue)) are also shown. Residues are numbered according to bovine rhodopsin.

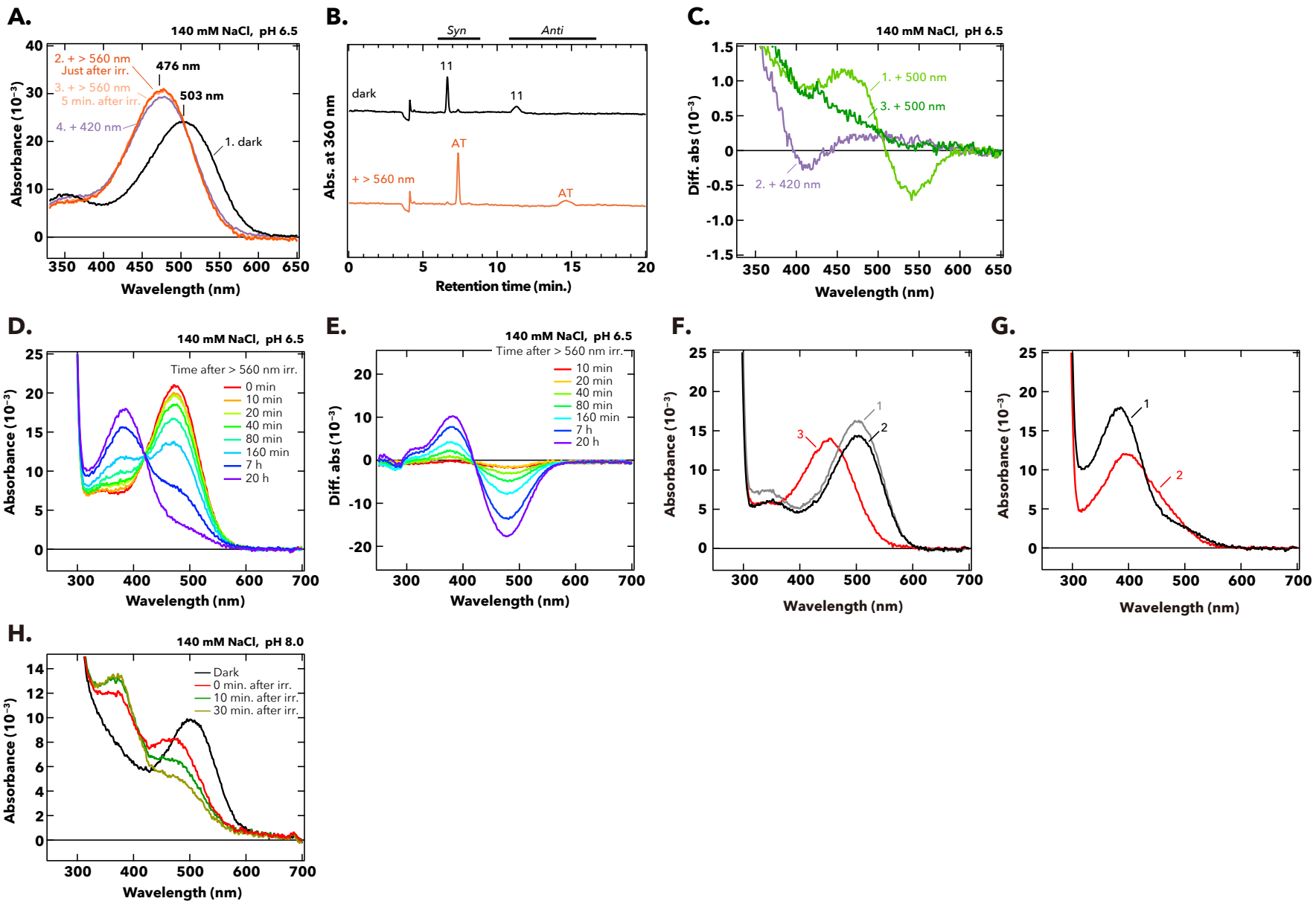
A.
140 mM NaCl, pH 6.5
2. + > 560 nm
Just after irr.
476 nm
3. + > 560 nm
5 min. after irr.
503 nm
4. + 420 nm
1. dark
Absorbance (10⁻³)
Wavelength (nm)
B.
Syn
Anti
11
dark
11
AT
+ > 560 nm
AT
Abs. at 360 nm
Retention time (min.)
C.
140 mM NaCl, pH 6.5
1. + 500 nm
3. + 500 nm
2. + 420 nm
Diff. abs (10⁻³)
Wavelength (nm)
D.
140 mM NaCl, pH 6.5
Time after > 560 nm irr.
0 min
10 min
20 min
40 min
80 min
160 min
7 h
20 h
Absorbance (10⁻³)
Wavelength (nm)
E.
140 mM NaCl, pH 6.5
Time after > 560 nm irr.
10 min
20 min
40 min
80 min
160 min
7 h
20 h
Diff. abs (10⁻³)
Wavelength (nm)
F.
1
2
3
Absorbance (10⁻³)
Wavelength (nm)
G.
1
2
Absorbance (10⁻³)
Wavelength (nm)
H.
140 mM NaCl, pH 8.0
Dark
0 min. after irr.
10 min. after irr.
30 min. after irr.
Absorbance (10⁻³)
Wavelength (nm)

919

920 **Fig. S3. Photo- and thermal reactions of wild type Antho2a.** (A) Absorption spectra of purified wild type Antho2a were measured at 0°C in the dark
921 (curve 1, black), after orange light irradiation (> 560 nm, curve 2 and curve 3, deep and pale orange), and after subsequent violet light irradiation (420
922 nm, curve 4, purple). Irradiation of wild type Antho2a with orange light shifted the absorption maximum from 503 nm in the dark (curve 1, black) to
923 476 nm in the photoproduct (curve 2 and curve 3, orange). Upon subsequent irradiation with 420 nm light (while the photoproduct was stable), the λ_{max}
924 of the photoproduct stayed at 476 nm, with only a slight decrease of the peak absorbance (curve 4, purple) possibly resulting from degradation of the
925 photoproducts upon light irradiation. (B) The configuration of retinal in wild type Antho2a before (black) and after (orange) irradiation with orange light
926 (> 560 nm) was analyzed with HPLC. Retinal was extracted in its oxime form. AT, all-*trans* retinal; 11, 11-*cis* retinal. (C) Difference spectra calculated
927 from the absorption spectra recorded before and after sequential irradiations with 500 nm and 420 nm light for crude extracts of detergent-solubilized
928 cell membranes expressing wild type Antho2a. Curve 1: Difference spectrum of after minus before 500 nm irradiation, showing a blue-shifted spectral
929 change indicative of photoproduct formation. Curves 2 and 3: Difference spectra of after minus before subsequent 420-nm light irradiation (curve 2),
930 and after minus before a second 500 nm light irradiation, following the 420 nm irradiation (curve 3). Neither condition resulted in spectral changes
931 consistent with regeneration of the dark state, indicating that Antho2a is not bistable under these conditions. (D) Changes in the absorption spectra of the
932 purified pigment of wild type Antho2a after irradiation with orange (>560 nm) light (with the sample kept in the dark at 0°C). Each colored curve
933 corresponds to a different incubation time after the light irradiation. (E) Difference spectra obtained by subtracting the spectrum of wild type Antho2a in
934 the dark from the spectra measured at different time points after irradiation (shown in D). (F, G) Acid denaturation of pigments before (dark state, F) and
935 after light irradiation (G). (F) Absorption spectra of wild type Antho2a in the dark were measured immediately after sample preparation at pH 6.5 (curve
936 1), and after incubation over night at 0°C (curve 2, pH 6.5) with subsequent addition of HCl to pH 1.9 (curve 3). (G) Absorption spectra of wild type
937 Antho2a incubated for 20 hours at 0°C following irradiation with orange light (> 560 nm), measured at pH 6.5 (curve 1) and after acidification to pH

938 1.9 (curve 2). When retinal binds to opsin via a Schiff base (protonated or deprotonated), acid denaturation traps the chromophore as a protonated Schiff
939 base, exhibiting absorption at λ_{max} ~440 nm. Acid denaturation of irradiated Antho2a (incubated for 20 hours post-irradiation) did not yield a product
940 with λ_{max} at ~440 nm (G, curve 2), whereas the dark state pigment after acidification displayed absorption at ~440 nm (F, curve 3). These results indicate
941 that Antho2a gradually releases retinal after light irradiation. (H) Absorption spectra of purified wild type Antho2a at pH 8.0, measured at 0°C before
942 (dark state; curve 1, black) and 0, 10, and 30 minutes after irradiation with orange light (> 560 nm; red, green, and yellow curves, respectively).

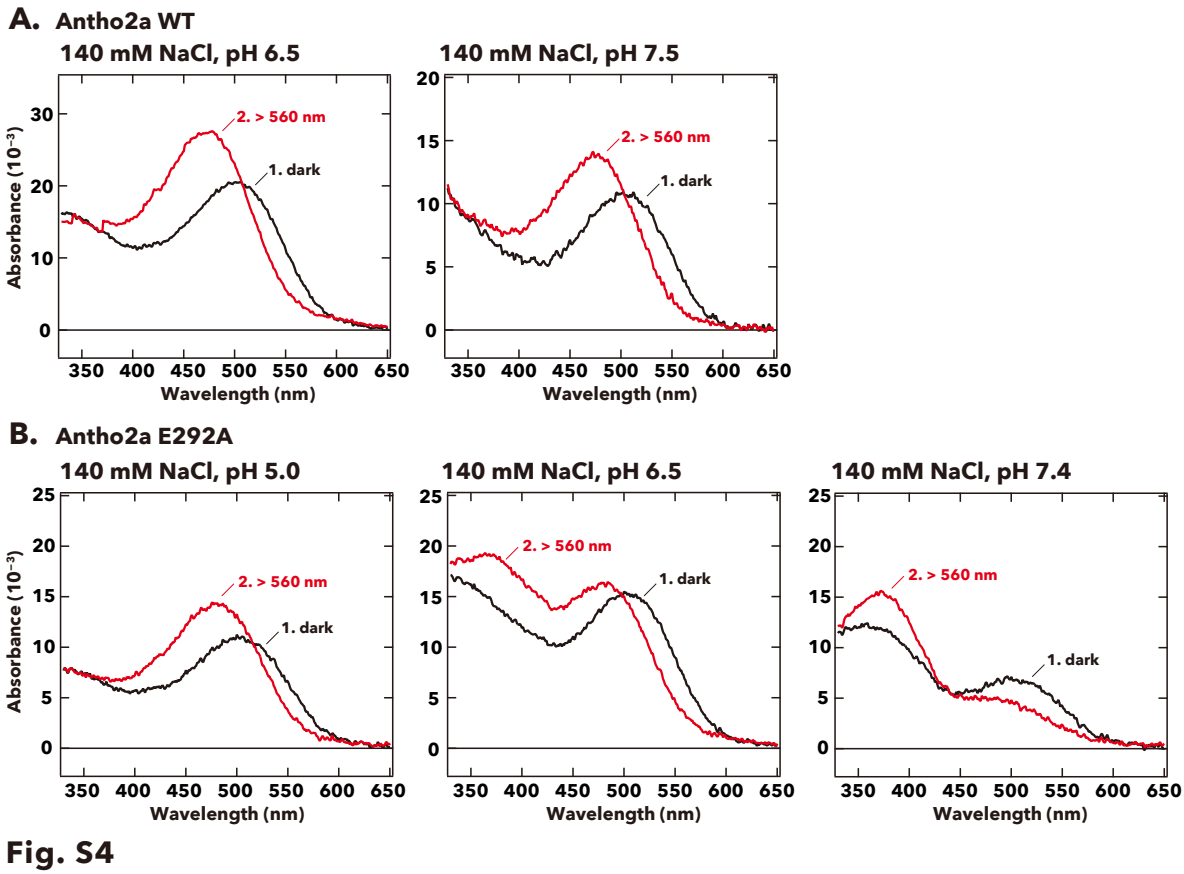

Fig. S4

Fig. S4. (A, B) Effect of pH on the absorption spectra of the dark state and photoproduct of (A) wild type Antho2a and (B) the E292A mutant at 140 mM NaCl. Each graph shows spectra before (curves 1, black) and after (curves 2, red) irradiation with orange (> 560 nm) light.

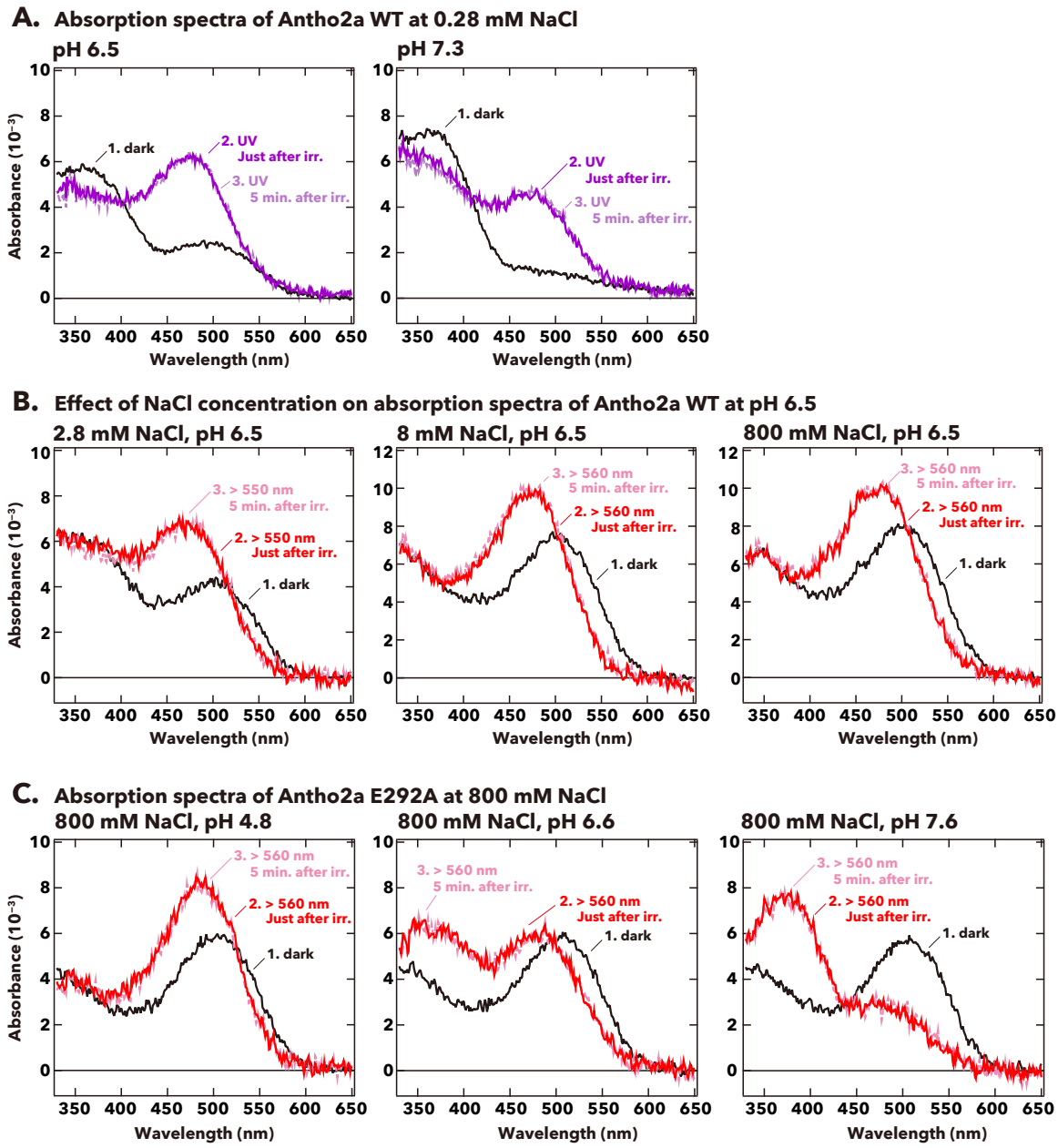

Fig. S5

Fig. S5. Effect of pH and NaCl concentration on absorption spectra of the dark states and photoproducts of Antho2a. (A) Absorption spectra of wild type Antho2a at 0.28 mM NaCl under different pH conditions (pH 6.5 and pH 7.3). (B) Absorption spectra of wild type Antho2a at pH 6.5 with varying NaCl concentrations (2.8 mM, 8 mM, and 800 mM). (C) Absorption spectra of the E292A mutant of Antho2a at 800 mM NaCl and different pH conditions (pH 4.8, pH 6.6, and pH 7.6). Each graph shows spectra before (curves 1, black) and after (curves 2, deep purple/red, and 3, pale

954 purple/pink) irradiation with UV light (< 410 nm, A) or orange light (> 550 nm or > 560 nm, B and C).
955 Curves 2 and 3 in each graph represent, respectively, the first measurement (immediately after
956 irradiation) and a subsequent measurement (< 5 min. after irradiation). The minimal change in the
957 absorption spectra over this time scale indicates that the spectra remain stable after irradiation.

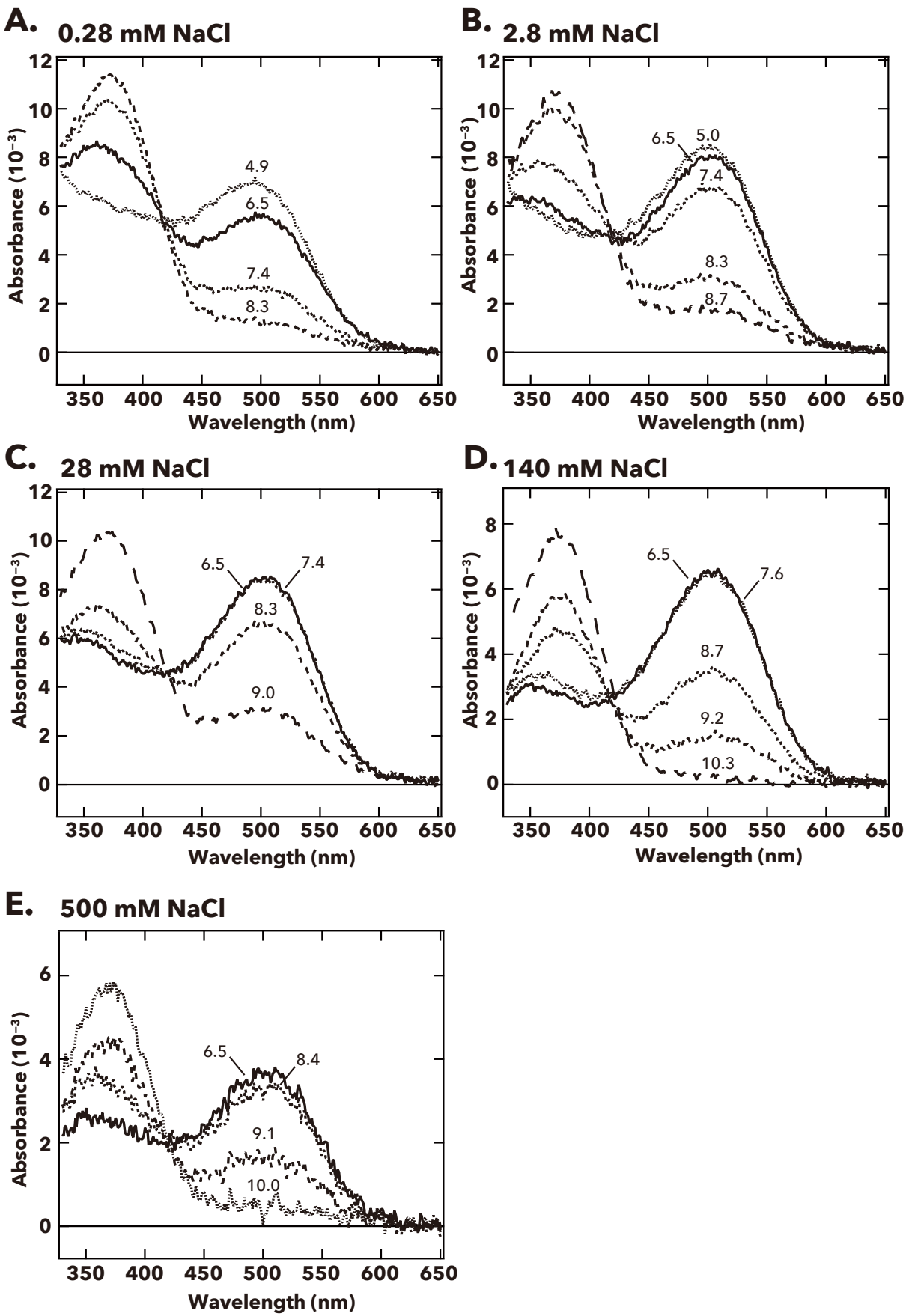
A.
0.28 mM NaCl
Absorbance (10⁻³)
Wavelength (nm)
4.9
6.5
7.4
8.3
B.
2.8 mM NaCl
6.5
5.0
7.4
8.3
8.7
C.
28 mM NaCl
6.5
7.4
8.3
9.0
D.
140 mM NaCl
6.5
7.6
8.7
9.2
10.3
E.
500 mM NaCl
6.5
8.4
9.1
10.0

958

959 **Fig. S6. pH-dependent changes in the absorption spectra of Antho2a WT at (A) 0.28 mM, (B) 2.8**
960 **mM, (C) 28 mM, (D) 140 mM, and (E) 500 mM Cl^- at 0°C.** The pH values of the solution,
961 measured right after each spectroscopic measurement, are indicated on the corresponding curves in
962 each graph.

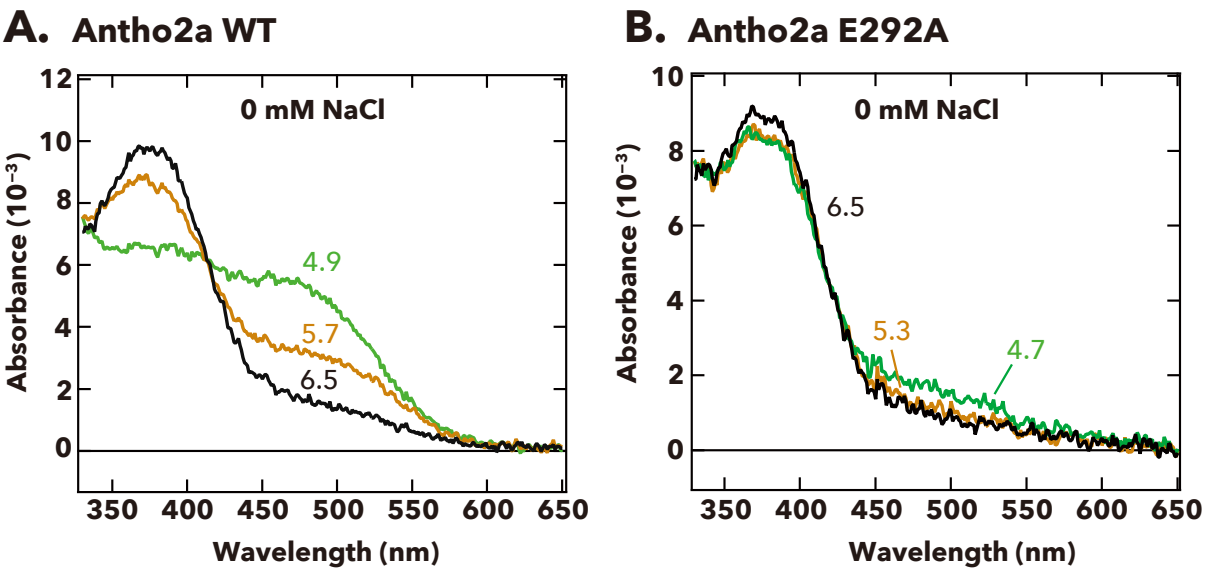

Fig. S7. pH-dependent changes in the absorption spectra of Antho2a WT and Antho2a E292A at 0 mM NaCl (containing 70 mM Na_2SO_4) at 0°C. The pH values at which the absorption spectra were measured are indicated on the corresponding curves.

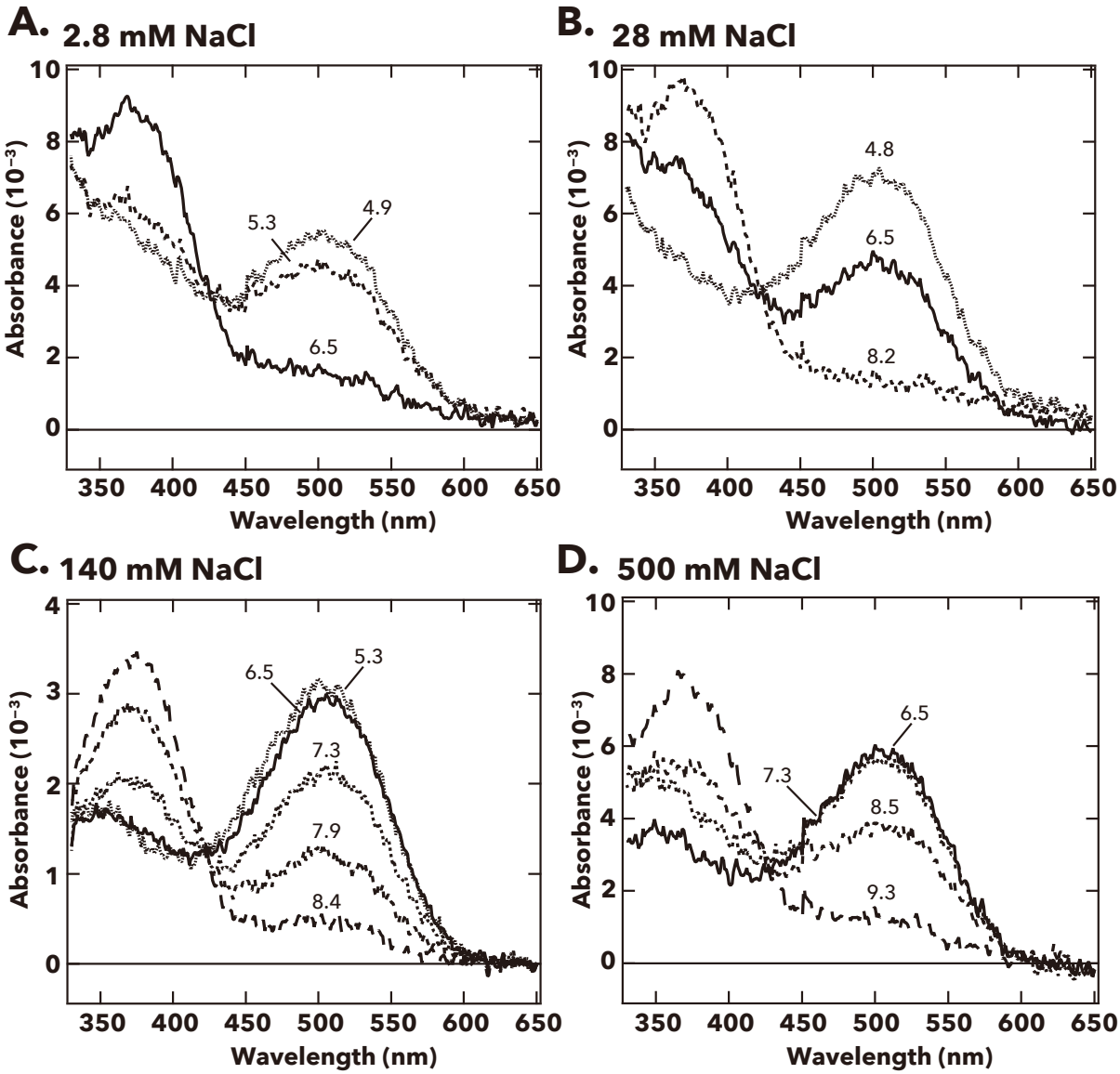

Fig. S8. pH-dependent changes in the absorption spectra of Antho2a E292A at (A) 2.8 mM, (B) 28 mM, (C) 140 mM, and (D) 500 mM Cl^- at 0°C. The pH values are indicated on the corresponding curves in each graph.

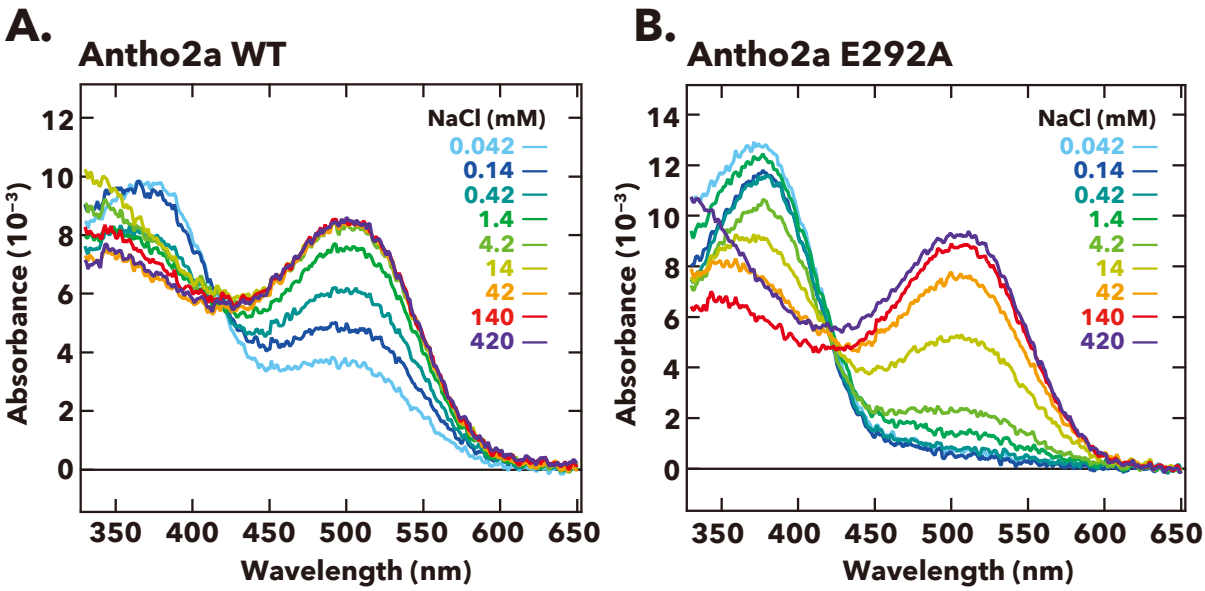

Fig. S9. Absorption spectra of (A) wild type Antho2a and (B) the Antho2a E292A mutant under different Cl^- concentrations at pH 6.5 and 0°C. Each color indicates a different concentration of Cl^-.

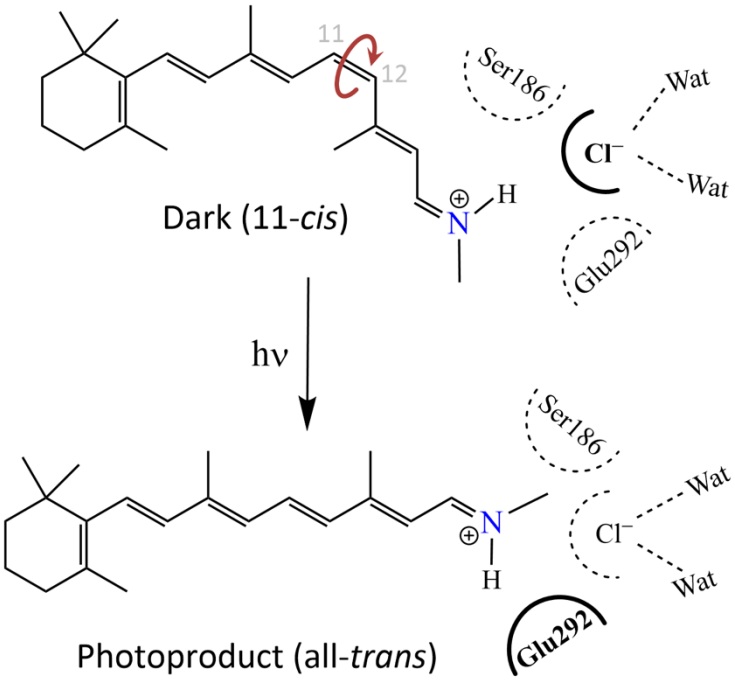

Fig. S10. Schematic drawing of the environment of the protonated Schiff base depicting the counterion switch from a chloride ion (top) to Glu292 (bottom) upon light activation.

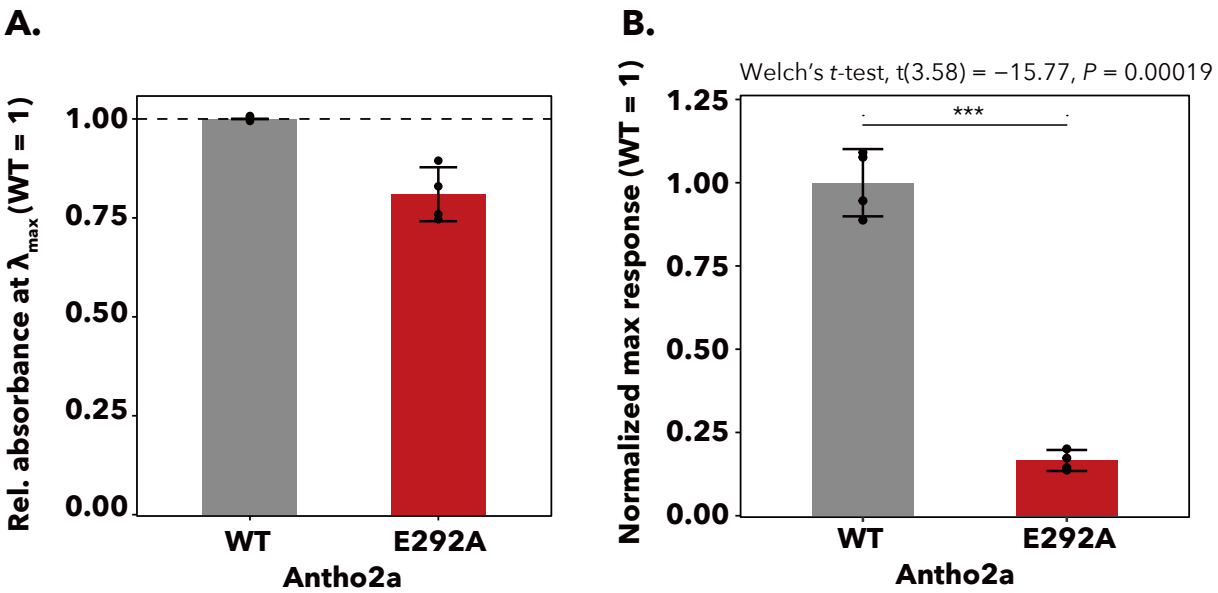

Fig. S11. Expression levels and normalized Ca^{2+} responses of wild type and E292A Antho2a. (A) The relative absorbances at λ_{max} (± 5 nm) of wild type (grey) and E292A (red) Antho2a are used as indicators of expression levels. The proteins were expressed and purified under identical conditions, and absorbance values of the E292A mutant were normalized to those of the wild type. Spectra were measured at 0°C, pH 6.5, and 140 mM NaCl. Each bar represents mean ± S.E.M. of n = 4 replicates from separate transfections in cultured cells. (B) Normalized maximum Ca^{2+} responses of HEK293S cells expressing wild-type Antho2a and the E292A mutant after irradiation with green light (510 nm). Responses were normalized to the expression levels shown in panel A. Each bar represents mean ± S.E.M. of n = 4 replicates from separate transfections in cultured cells. Statistical evaluation of the normalized Ca^{2+} responses for wild type Antho2a versus the E292A mutant was conducted using a Welch's *t*-test (two-sided). ***$P < 0.001$.